WEATHER ON OTHER WORLDS IV: IN-DEPTH STUDY OF PHOTOMETRIC VARIABILITY AND RADIATIVE TIMESCALES FOR ATMOSPHERIC EVOLUTION IN FOUR L DWARFS

by

Davin C. Flateau

A Thesis Submitted to the Faculty of the

DEPARTMENT OF PLANETARY SCIENCES

In Partial Fulfillment of the Requirements

For the Degree of

MASTER OF SCIENCE

In the Graduate College

THE UNIVERSITY OF ARIZONA

2015

STATEMENT BY AUTHOR

This thesis has been submitted in partial fulfillment of requirements for an advanced degree at the University of Arizona and is deposited in the University Library to be made available to borrowers under rules of the Library.

Brief quotations from this thesis are allowable without special permission, provided that accurate acknowledgment of the source is made. Requests for permission for extended quotation from or reproduction of this manuscript in whole or in part may be granted by the head of the major department or the Dean of the Graduate College when in his or her judgment the proposed use of the material is in the interests of scholarship. In all other instances, however, permission must be obtained from the author.

SIGNED: Davin C. Flateau

Davin C. Flateau

APPROVAL BY THESIS DIRECTOR

This thesis has been approved on the date shown below:

Dániel Apai
Assistant Professor, Department of Planetary Sciences
and Department of Astronomy

Date

ACKNOWLEDGEMENTS

This work is based in part on observations made with the Spitzer Space Telescope, obtained from the NASA/ IPAC Infrared Science Archive, both of which are operated by the Jet Propulsion Laboratory, California Institute of Technology under a contract with the National Aeronautics and Space Administration. This research has benefitted from the SpeX Prism Spectral Libraries, maintained by Adam Burgasser at http://pono.ucsd.edu/ adam/browndwarfs/spexprism. The author wishes to acknowledge the faculty and staff of the University of Arizona Department of Planetary Sciences/Lunar and Planetary Laboratory for their guidance and assistance.

DEDICATION

For Joori and Kyu

TABLE OF CONTENTS

TABLE OF CONTENTS – *Continued*

LIST OF FIGURES

LIST OF FIGURES – *Continued*

LIST OF FIGURES – *Continued*

LIST OF FIGURES – *Continued*

LIST OF TABLES

ABSTRACT

Rotational phase mapping of brown dwarfs allows exploration of different cloud and photospheric properties within the same atmospheres, allowing a separation of these parameters from global parameters, such as composition, surface gravity, and age. This work presents an in-depth characterization of high SNR light curves from the Spitzer Space Telescope with up to 13 hours of continuous monitoring of four dwarfs spanning the L3 to L8 spectral type. An exhaustive exploration of currently available state-of-the-art models explains the observed color changes for two of these dwarfs with a linear combination of two model cloudy surfaces differing in effective temperature, cloud opacity and vertical mixing. Using state-of-the-art purely radiative convective atmospheric models, we calculate basic radiative timescales for temperature perturbations in the atmosphere, and consider the effects of dynamics on these timescales. Along with dynamical atmospheric advection timescales, we discuss the relationships between model timescales and the observed light curve evolution.

CHAPTER 1

INTRODUCTION

Brown dwarfs are an excellent laboratory for studying cool, cloudy atmospheres that overlap in physical and chemical properties with extrasolar planets. Brown dwarfs are typically free-floating objects that are not irradiated by a host or companion star, making them easier to study than both close-in and widely-separated planets. The relatively recent observational discovery and characterization of thousands of brown dwarfs throughout a range of temperatures has provided an opportunity to study many different characteristics of cool, cloudy atmospheres in detail. With recent advances in infrared detectors and telescopes, brown dwarfs present the opportunity to probe the composition of complex atmospheric cloud structures, as well as characterizing rapid changes in cloud properties due to dynamical advection and thermodynamic processes. The characterization of a wide variety of brown dwarf atmospheres can provide important constraints to the physical and chemical models of solar system and extrasolar planetary atmospheres.

1.1 Brown Dwarf Overview

The theoretical existence of free-floating substellar objects formed from the gravitational collapse of molecular gas with insufficient mass to sustain hydrogen fusion was predicted as early as the 1960s (Hayashi and Nakano 1963; Kumar 1963). But advances in optical and infrared instrumentation sensitivity would take another 30 years to lead to the announcement of the first generally accepted confirmed detection of a brown dwarf (Gliese 229 B, Nakajima et al. 1995). Since then, thousands of brown dwarfs have been identified with the help of large surveys, including the Deep Near-Infrared Southern Sky Survey (DENIS, Epchtein et al. 1999), the Sloan Digital Sky Survey (SDSS, York et al. 2000) and the Two-Micron All-Sky Survey (2MASS,

Skrutskie et al. 2006). Observed spectral features in these objects throughout various temperature regimes led to their subsequent classification into four spectral types, late M ($T_{eff} = 3500 - 2100$ K, Kirkpatrick et al. 1991), L ($T_{eff} = 2100 - 1300$ K, Kirkpatrick et al. 1999), T ($T_{eff} = 1300 - 500$ K, Burgasser et al. 2006) and "room temperature" (and below) Y dwarfs (< 500 K, Cushing et al. 2011). Despite their historical elusiveness to detection, recent estimates of brown dwarf number densities for the local stellar neighborhood (< 26 light years) indicate the existence of perhaps one brown dwarf for every four stars (Andersen et al. 2008; Kirkpatrick et al. 2011; Burningham et al. 2013).

1.2 Brown Dwarf Evolution

During initial contraction of the brown dwarf, gas density at the core is high enough for free electrons to fill the lower Fermi energy states, creating pressure from the partially degenerate electron gas that balances the gas' gravitational force, keeping the brown dwarf's radius near that of Jupiter (7×10^7 m). Brown dwarfs will typically fuse deuterium into lithium-3 for a few Myr before deuterium depletion halts the reaction. More massive brown dwarfs ($M > 65$ M_{Jup}) can additionally fuse lithium (e.g. Dantona and Mazzitelli 1985; Stringfellow 1989). After nuclear reactions have ceased, the brown dwarf continues to radiate away energy as it cools.

As the dwarf cools, its T_{eff} passes through the condensation points of various chemical compounds. The spectral energy distribution (SED) of the dwarf is subsequently altered as gas-phase absorption features due to certain species (e.g. TiO, VO) disappear as they condense into the cooler atmosphere, while the spectral features of condensates including silicates become visible. As the brown dwarf cools, it evolves through the M-L-T-Y sequence. But since brown dwarfs can form with various masses, thus starting off with different thermal energy from contraction, they can begin their lives in different places along the M-L-T-Y sequence. This creates an ambiguity between the observed luminosity of the brown dwarf and its age, mass and radius, which are calculated values. Additionally determining the object's

surface gravity ($g = GM/R^2$, where G is the universal gravitational constant, M the mass and R the radius of the dwarf, usually ranging from $10 - 3000\text{m/s}^2$) with techniques such as spectral model fitting, can be an important characteristic used to resolve this ambiguity in evolutionary models (Saumon and Marley, 2008).

1.3 Brown Dwarf Spectra

Figure 1.1 shows representative 0.65–14.5 μm spectra for brown dwarf spectral types in comparison to Jupiter. With decreasing T_{eff}, the general blackbody-like shape of the late M-dwarf's SED is altered by increasingly prominent molecular absorption bands. The warmest late-M type dwarfs are characterized by bands from metal-hydrides and metal-oxides such as TiO and FeH, which are incorporated into grains. In L dwarfs, lower temperatures allow iron and silicate grains to produce optically thick clouds, which can obscure the molecular absorption bands from gases. These condensate clouds also significantly redden the near-infrared JHK colors of these dwarfs with decreasing temperature through later L types. Near the L and T spectral type boundary ($\sim 1,400$ K), a color shift toward the blue occurs over a narrow temperature interval (Dahn et al. 2002; Tinney et al. 2003; Vrba et al. 2004), and has been explained by the onset of patchiness in the global cloud structure (e.g., Ackerman and Marley 2001; Burgasser et al. 2002; Saumon and Marley 2008; Marley et al. 2010; Radigan et al. 2012; Apai et al. 2013). In T dwarfs, the CH_4 bands become more prominent from their first appearance in mid L dwarfs (Noll et al., 2000), and together with the sunken condensate clouds and collision-induced H_2 opacity between 2.0–2.4 μm (for >T5), continue the blueward shift of NIR colors for cooler dwarfs, even as the gradual cooling of the dwarf would naturally progress the object towards redder NIR colors. Jupiter's spectra < 4 μm are dominated by scattered sunlight altered by NH_3 and CH_4 absorption features.

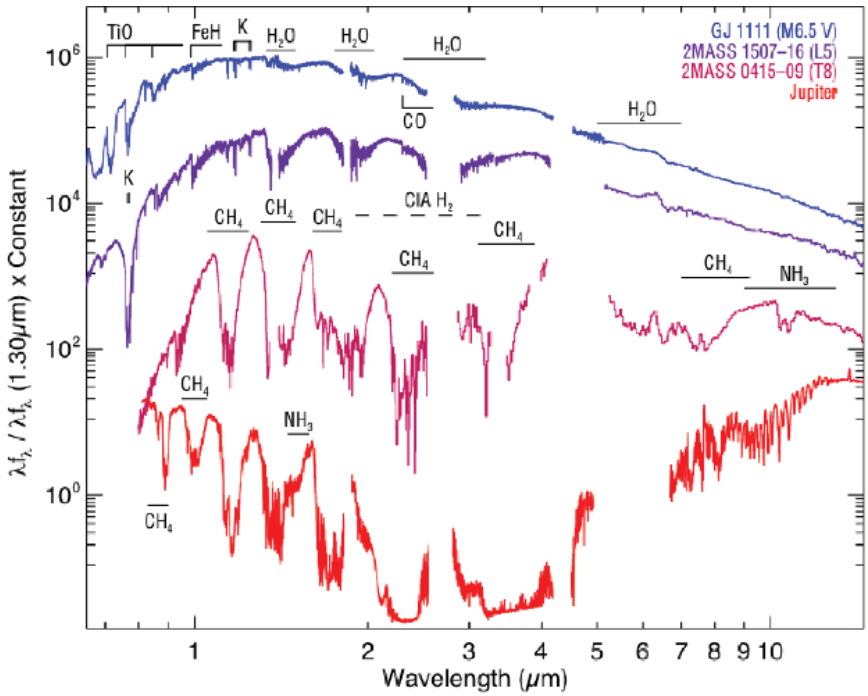

Figure 1.1 Representative spectra spanning the optical to infrared (0.65–14.5 μm) for the spectral sequence of brown dwarfs and Jupiter. The spectra are normalized to unity at 1.3 μm and an offset applied for clarity. Significant molecular absorption bands that characterize the spectra are labeled, including CO, TiO, FeH, CH_4, H_2 (dashed lines represent a broad, smooth absorption over these regions), NH_3 and H_2O. Dwarf spectral data are from Cushing et al. (2006); Jupiter data are from Rayner et al. (2009) and Kunde et al. (2004). Figure from Marley and Leggett (2009).

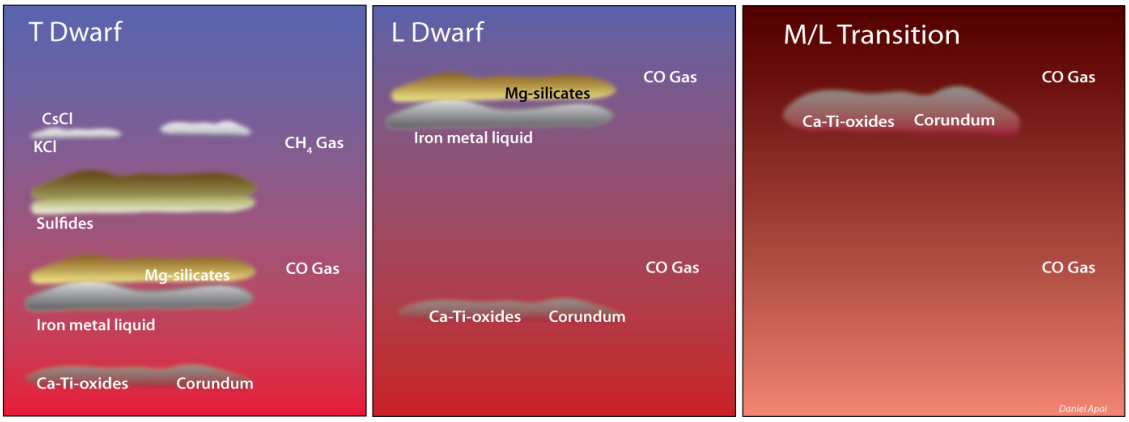

Figure 1.2 A schematic of condensate clouds as calculated for progressive pressure and temperature layers spanning from T dwarfs to the warmest (spectral type M) brown dwarfs. Clouds of various condensate species form at specific levels of pressures and temperatures, falling lower into the atmosphere as the dwarf cools. Figure courtesy of Dániel Apai.

1.4 Condensate Clouds in Brown Dwarfs

Understanding the chemistry and structure of condensate clouds plays a critical role in the L dwarfs' observed SED and colors. Optically opaque cloud layers at altitude can absorb flux from deeper, warmer layers, and can be disrupted or altered by processes including atmospheric dynamics, thermodynamic activity, and chemical processes. These processes may create a global patchwork of layered clouds of varying properties including optical depth and grain sizes, that shape the observed SED from the dwarf (Marley et al., 2010). Figure 1.2 shows a schematic of how the progression of pressure and temperature through a brown dwarf's atmosphere allows the condensation of cloud decks of distinct chemical species. Higher temperatures and pressures allow the formation of grains of refractory compounds like metal-oxides and silicates, while lower pressures and temperatures at higher altitudes allow volatile species to condense such as chlorides (Ackerman and Marley 2001; Lodders and Fegley 2006). For decreasing dwarf T_{eff}, these clouds decks descend further into the atmosphere, following higher pressures and temperatures.

Modeling of clouds has been notoriously difficult, but there has been steady

progress in modeling the emergent SED from brown dwarf condensate clouds towards state-of-the-art models that have had success in reproducing the NIR colors and spectra of L dwarfs (e.g. Lewis 1969; Fegley and Lodders 1994; Lunine et al. 1989; Marley et al. 1999). In the models of Ackerman and Marley (2001), condensation clouds are treated as longitudinally homogenous, whose vertical extent is balanced between the downward transport of sediment and the upward transport of vertical mixing of both condensate and vapor according to

$$- K_{zz} \frac{\partial q_t}{\partial z} - f_{\rm sed} w_* q_c = 0 \tag{1.1}$$

where K_{zz} is the vertical eddy diffusion coefficient, q_c and q_v are moles of condensate and vapor (respectively) to moles of atmosphere, q_t is total moles of condensate and vapor ($q_t = q_c + q_v$), and w_* is the convective velocity scale. The critical free parameter in this model is the sedimentation efficiency factor $f_{\rm sed}$. Large values of $f_{\rm sed}$ correspond to rapid particle growth resulting in large mean particle sizes. Condensates quickly settle in this case, leading to physically and optically thin clouds. When $f_{\rm sed}$ is small, particles grow more slowly, do not settle out, leading to a larger atmospheric condensate load and thicker clouds. The cloud model is fully coupled with the radiative transfer and self-consistent with the (P, T) structure of the model. These models have been used successfully in modeling the $J - K$ color shift of the L/T transition (Saumon and Marley, 2008), and in producing model spectra that have matched well to the observed NIR spectra of L dwarfs (Cushing et al., 2008).

1.5 Periodic Photometric Variability due to Heterogenous Clouds

The idea of disrupted clouds in an L/T dwarf led to the testable hypothesis that a dwarf's rotation could produce a modulated photometric variability as the heterogenous cloud structure rotates through the field of view. While hot and cold spots in the atmosphere due to the coupling of a dwarfs' magnetic field with the atmosphere may be a possible mechanism for modulated photometric variability in

hotter, more magnetically-active late M or early L dwarfs, the neutral atmospheres of L and T dwarfs are generally considered too electrically resistive for this kind of coupling (e.g., Mohanty et al. 2002; Chabrier and Küker 2006), although there have been some examples of observed flaring activity in radio bandpasses in objects as cool as T dwarfs (e.g., Route and Wolszczan 2012).

Early searches for this variability, primarily with ground-based instruments in optical red or NIR wavelengths, over timescales ranging from minutes to weeks, led to largely ambiguous detections or detections that were not found on followup observations (e.g. Bailer-Jones and Mundt 2001; Enoch et al. 2003; Koen 2005a,b; Clarke et al. 2002a; Khandrika et al. 2013; Wilson et al. 2014, reevaluated in Radigan 2014). The first tentative detection of photometric periodic variability was the L2 dwarf Kelu-1 (Clarke et al., 2002b) with a 1.1% peak-to-peak amplitude at 860 nm, and a 1.8 h period. Although followup observations did not detect the same variability in the I band, the Hα line intensity was observed to vary in intensity in the same period (Clarke et al., 2003). The first unambiguous detection a variable brown dwarf was the T2.5 dwarf SIMP J013656.5+093347, with a $\Delta J = 50$ mmag and a period of 2.4 h (Artigau et al., 2009). Subsequent notable detections include the T1.5 dwarf 2MASS J21392676+0220226, with a maximum 26% variability in J and a 7.7 h period (Radigan et al., 2012), and the T0.5 dwarf SDSS J105213.51+442255.7, with a 6% maximum variability and a 3 h period (Girardin et al., 2013).

In addition to ground-based studies, Spitzer Space Telescope IRAC and HST WFC3 instruments (Buenzli et al. 2012; Heinze et al. 2013; Apai et al. 2013) observed brown dwarf variations over 3.6 and 4.5 μm bands, and the 1.1–1.7 μm spectral range (time-resolved spectroscopy), respectively. Apai et al. (2013) concluded that J and H band color changes and spectral variations in two L/T transition dwarfs could be explained by a heterogeneous mix of low-brightness, low-temperature thick clouds and brighter, warmer, thin clouds, with the absence of deep cloud holes. Possible mechanisms in that study for the change in cloud properties were suggested to be large-scale vertical mixing and circulation. Subsequently, Buenzli et al. (2015a,b) successfully described the mean spectrum and relative amplitudes of Luhman 16A

and B, two variable L/T transition dwarfs as observed with HST between 1.1–1.66 and 0.8–1.15 μm (respectively), with sets of two-component cloud models that linearly combined a warmer, thinner cloud with a cooler, denser cloudy model. Yang et al. (2015) found that two L5 dwarfs with 1.1–1.7 μm spectral variability as observed with HST were explained with models that utilized a spatially-variable high-altitude haze layer that resided at very low pressures above the condensate clouds.

The Apai et al. (2013) and Buenzli et al. (2012) works utilized their observations at multiple wavelengths to find pressure-dependent phase shifts in the periodic photometric variability for a T6.5 dwarf, but no phase shifts for two T2 dwarfs. These studies show how cloud structures can be explored vertically and longitudinally with time-resolved observations. The Buenzli et al. (2014) and Metchev et al. (2015) HST and Spitzer surveys show that most, if not all brown dwarfs have heterogeneous cloud cover and show rotational modulations if observed with sufficient precision.

1.6 Dynamic and Thermal Modeling

Dynamic and thermal modeling have been important in understanding mechanisms of cloud formation and stability as well as the role of possible temperature perturbations could play in understanding periodic photometric variability. Freytag et al. (2010) used a 2-D radiative hydrodynamic model to show that gravity wave propagations in brown dwarf atmospheres are common above the radiative-convective boundary, and should play an important role in cloud formation and evolution, at least on small scales. Showman and Kaspi (2013) utilized 3-D global models to explore convection and global circulation in dwarfs. This work showed that stratified turbulence and flows resulting from atmospheric waves could result in horizontal temperature variations of up to $\sim$50K. This model also predicts large-scale organization of the atmospheric flow, and wind speeds of tens to hundreds of m/sec. Flow organization will modulate the cloud structure, leading to large-scale patchiness in the cloud structure as necessary to explain variability measurements. Robinson and

Marley (2014) investigated the role that the aforementioned atmospheric temperature variations could play as a possible source of observed NIR variations in brown dwarfs. This work showed that in a purely radiative non-grey atmosphere, thermal perturbations at pressures greater than 10 bar propagate to the upper atmosphere by radiative heating through the windows in NIR water opacity. Such radiative feedback mechanisms through various atmospheric depths are important for understanding other possible sources of brown dwarf variability. Zhang and Showman (2014) performed one-layer shallow-water calculations of the atmospheric flow to determine the extent to which small-scale turbulent forcing, associated with convective perturbations at the radiative-convective boundary, can lead to formation of atmospheric vortices and zonal jets analogous to those occurring on Jupiter and Saturn. Their models showed that, at long radiative time constants, zonal jets can form, analogous to those on Jupiter. However, when the radiative time constant is sufficiently short, the radiation damps the atmospheric turbulence before it can organize into jets, and in this case the circulation consists primarily of quasi-isotropic turbulence without strong zonal jets.

In exploring the possible sources of periodic photometric variability, a variety of complex interactions must be considered, from heterogeneous cloud properties and surface coverage, to the dynamic and thermal properties of the atmosphere. With high-precision uninterrupted NIR light curves spanning multiple wavelengths over multiple dwarf rotation periods, we can assess the atmospheric origins of this variability by constraining the cloud coverage, opacity and T_{eff} differences of condensate clouds in the dwarf. Such light curves can also reveal the timescales for evolution of the periodic photometric variability. This allows us to discern possible origins for this evolution by comparing these times to results from state-of-the-art radiative and atmospheric dynamic models.

CHAPTER 2

STATEMENT OF WORK

In my research preceding this thesis, I contributed to five refereed publications in The Astrophysical Journal closely aligned with the research summarized in this thesis (listed below). Specifically, for Paper 1, I managed spacecraft observations, created data reduction and characterization techniques, and conducted or assisted with ground follow-up observations. In Paper 2, I reduced the Spitzer data and characterized amplitudes and periods, and was involved in the target selection for the two dwarfs that were the subject of the study. In Paper 3, I helped compare the variable targets from HST with their variability from our Spitzer program. In Paper 4, I was involved in managing spacecraft observations as well as assisting in Spitzer data reduction and overall Spitzer program execution, and in Paper 5, I reduced the Spitzer data for the target object which had simultaneous HST observations.

In this thesis, I am presenting a work on four L dwarfs from the Weather on Other Worlds Spitzer Exploration Program. The work described is being submitted for publication in The Astrophysical Journal. This thesis is based on a work that will have multiple authorship, with myself leading the investigation, and performing spacecraft observation planning, data reduction and analysis. This work contains contributions from Dániel Apai (University of Arizona, overall guidance and general contributions), Stanimir Metchev (Western University, Principal Investigator for Weather on Other Worlds, general contributions), Mark Marley (NASA Ames Research Center, spectral and flux models), Didier Saumon (Los Alamos National Laboratory, spectral and flux models), Adam Showman (University of Arizona, atmospheric dynamics discussions), Aren Heinze (Institute for Astronomy, advice on data analysis), Kelle Cruz (Hunter College, contributed spectrum), Nikole Lewis (Massachusetts Institute of Technology, data reduction techniques), and Étienne Artigau (Université de Montréal, general contributions).

Publications:

1. Metchev, S. A., A. Heinze, D. Apai, **D. Flateau**, J. Radigan, A. Burgasser, M. S. Marley, É. Artigau, P. Plavchan, and B. Goldman (2015). Weather on Other Worlds. II. Survey Results: Spots are Ubiquitous on L and T Dwarfs. ApJ, 799, 154.

2. Yang, H., D. Apai, M. S. Marley, D. Saumon, C. V. Morley, E. Buenzli, É. Artigau, J. Radigan, S. Metchev, A. J. Burgasser, S. Mohanty, P. J. Lowrance, A. P. Showman, T. Karalidi, **D. Flateau**, and A. N. Heinze (2015). HST Rotational Spectral Mapping of Two L-type Brown Dwarfs: Variability in and out of Water Bands indicates High-altitude Haze Layers. ApJ, 798, L13.

3. Buenzli, E., D. Apai, J. Radigan, I. N. Reid, and **D. Flateau** (2014). Brown Dwarf Photospheres are Patchy: A Hubble Space Telescope Near-infrared Spectroscopic Survey Finds Frequent Low-level Variability. ApJ, 782, 77.

4. Heinze, A. N., S. Metchev, D. Apai, **D. Flateau**, R. Kurtev, M. Marley, J. Radigan, A. J. Burgasser, É. Artigau, and P. Plavchan (2013). Weather on Other Worlds. I. Detection of Periodic Variability in the L3 Dwarf DENIS- P J1058.7-1548 with Precise Multi-wavelength Photometry. ApJ, 767, 173.

5. Buenzli, E., D. Apai, C. V. Morley, **D. Flateau**, A. P. Showman, A. Burrows, M. S. Marley, N. K. Lewis, and I. N. Reid (2012). Vertical Atmospheric Structure in a Variable Brown Dwarf: Pressure-dependent Phase Shifts in Simultaneous Hubble Space Telescope-Spitzer Light Curves. ApJ, 760, L31.

CHAPTER 3

OVERVIEW

In the following chapter, we will describe the observational background for 4 variable L dwarfs from the Weather on Other Worlds program (hereafter WoW), and summarize the observational history and previous searches of variability in these targets. In Chapter 4, we describe the data reduction methods for our warm Spitzer observations, including correcting for intrapixel sensitivities. In Chapter 5, we analyze the reduced photometry for our targets, extracting relative amplitudes, rotation periods, and examine light curve shapes. We also present a possible correlation between the Ch1 and Ch2 light curves in SDSS0107, and present the results of absolute photometry of our dwarfs. In Section 5.4.1, we examine the light curves for any observed evolution during the length of the observations, and in Chapter 6, match model spectra with archived SpeX spectra and observed Spitzer fluxes for our targets, determining atmospheric parameters that include the cloud opaqueness of observed atmospheric layers and gravity. Also in Chapter 6, we investigate how pairs of models of cloudy surfaces can be used in describing the colors changes of our dwarfs due to variability. Finally, we explore the behavior of theoretical thermal perturbations at atmospheric depths and atmospheric dynamics as a cause of our variability and light curve evolution.

3.1 Target Selection

This work represents results from the Weather on Other Worlds program, a Spitzer Space Telescope Cycle 8 Exploration Science program (GO 80179, Metchev et al. 2011, 2015), utilizing IRAC channel 1 ([3.6], Ch1) and channel 2 ([4.5], Ch2) during the spacecraft's post-cryogenic period known as "warm Spitzer". The WoW campaign was an extensive campaign to characterize the variability in an unbiased

selection of 44 non-binary dwarfs ranging from L3 to T8, including both typical and peculiar objects throughout this spectral type range. Most targets were continuously monitored for 7–14 hours to capture at least two typical brown dwarf rotation periods (Metchev et al., 2015) in Ch1, and one additional period in a 6-7 hour observation in Ch2. Some targets in the 873 hour survey have simultaneous or near-simultaneous ground-based observations in I or JHK bands. The survey results in Metchev et al. (2015) include that, after correcting for sensitivity, $80\%^{+20\%}_{-27\%}$ of L dwarfs are photometrically variable with a relative amplitude $\geq$ 0.2%, and $36\%^{+26\%}_{-17\%}$ of T dwarfs vary by $\geq$ 0.4%. That work also found that a third of variable L dwarfs have irregular light curves, which they attributed to multiple atmospheric spots evolving over a single rotation. The work also revealed that a third of all of the target dwarfs have rotation periods $>$ 10 h, and presented a tentative association between low surface gravity and high-amplitude variability among L3–L5.5 dwarfs. Previous findings of this program were included in Heinze et al. (2013), which described the L3 dwarf DENIS-P J1058.7-1548, which was found to have a peak-to-trough variability amplitude of $0.388\% \pm 0.043$ with P=$4.25^{+0.26}_{-0.16}$ h, and Heinze et al. (2015) which described the search for I–band variability of the Spitzer program's T-dwarfs, suggesting that high-amplitude photometric variability for T–dwarfs is is more common in the optical than at longer wavelengths.

For this study, we chose to investigate a subsample of WoW targets spanning mid-L spectral types (L3–L8), whose atmospheres are characterized by persistent condensate clouds, as opposed to the patchy clouds expected in later L and early T-type dwarfs. This provides a basic level of atmospheric homogeneity in our sample when creating modeling assumptions about recreating observed variability. Within that sample, we included objects with a variety of previously determined gravities. We also included one object that has been previously identified as an active radio emitter, which gives our sample an atmosphere that has the possibility of magnetically-induced spots on the surface, allowing us to investigate whether cloud modeling results differ for that object. We also chose objects in this sample that have some of largest SNR for relative light curve am-

plitudes in both channels, enabling us to robustly determine periods and amplitudes for our objects. Our radio-emitting dwarf has the added advantage in this sample of having a very small amplitude in both Spitzer channels, enabling us to investigate the effects of very low amplitudes on our modeling approach. Our targets are the L5.5 dwarf SDSSpJ010752.33+004156.1 (hereafter SDSS0107), the known radio-emitting L3.5 dwarf 2MASSWJ0036159+182110 (2M0036), the low-gravity L6 dwarf 2MASSIJ0103320+193536 (2M0103) and the low gravity L3 dwarf 2MASSWJ2208136+292121 (2M2208).

Compiled literature data on our four targets can be found in Table 3.1. A brief summary of each's object's key properties and results from previous searches for variability follows.

3.2 The Young, Low-Gravity L3 Dwarf 2M2208

2M2208 was discovered by Kirkpatrick et al. (2000), and was identified as one of only two spectroscopically peculiar L dwarfs at the time. Subsequent $0.6 - 1\mu$m Subaru FOCAS spectra identified 2M2208 as a low gravity L-dwarf due to weaker K I doublets and hydride bands of CaH, CrH, and FeH when compared to other L dwarfs of its type (Kirkpatrick et al., 2008), and identified it as spectral type L2. That work also found strong spectral similarity to the L-dwarf G 196-3B, which has an age estimate based on that object's M2.5 dwarf primary companion between 20 and 300 Myr (Kirkpatrick et al., 2001), thereby estimating 2M2208's age as $\sim$ 100 Myr. Cruz et al. (2009) reclassified 2M2208 as an L3γ dwarf, (γ designating low gravity) and concluded that based on the behavior of low-gravity features of the spectra of late M-dwarfs, 2M2208 had an age close to $\sim$10 Myr. Allers and Liu (2013) confirm the low gravity of this object in their study of ultracool field dwarfs using gravity-sensitive indices based on FeH, VO, K I, Na I, and H–band continuum shapes. Gagné et al. (2014) concluded that 2M2208 has a modest probability (10.1%) of being a $9 - 11 M_{\rm Jup}$ *planemo* member of the β Pictoris moving group. Enoch et al. (2003) searched for variability in Ks band in 2M2208 during a 29 day

Table 3.1. Target Properties and Observation Log

Quantity	SDSS0107	2M0036	2M0103	2M2208	Source
α (J2000)	01^h 07^m $52^s.42$	00^h 36^m $16^s.17$	01^h 03^m $32^s.03$	22^h 08^m 13^s $.63$	3,3,3,3
δ (J2000)	$+00^d$ 41^m $56^s.3$	$+18^d$ 21^m $10^s.4$	$+19^d$ 35^m $36^s.1$	$+29^d$ 21^m $21^s.5$	3,3,3,3
J	15.824 ±0.058	12.466 ±0.027	16.288 ±0.080	15.797 ±0.085	3,3,3,3
H	14.512 ±0.039	11.588 ±0.029	14.897 ±0.056	14.793 ±0.071	3,3,3,3
K	13.709 ±0.044	11.058 ±0.021	14.149 ±0.059	14.148 ±0.073	3,3,3,3
$J-H$	1.31 ±0.070	0.878±0.040	1.391±0.098	1.004±0.111	3,3,3,3
$H-K$	0.803 ±0.059	0.530 ±0.036	0.748 ±0.081	0.748 ±0.102	3,3,3,3
SpT	L5.5 (NIR)	L3.5 (Opt)	L6 (Opt)	L3γ (Opt)	4,7,6,8
d (pc)	15.59 ±1.10	8.76 ±0.06	21.90 ±3.55	47.22 ±1.56	7,9,6,5
Observing Log					
Ch1 Start (UT)	10 Oct 2012 15h06m	09 Oct 2012 16h14m	15 Oct 2012 06h06m	16 Sep 2012 10h31m	
Ch1 Length (h)	13.83	7.88	13.83	13.83	
Ch1 $t_{exp}(s)$	12	12	12	12	
Ch1 N_{exp}	3801	2166	3801	3801	
Ch2 Start (UT)	11 Oct 2012 05h09m	10 Oct 2012 00h11m	15 Oct 2012 20h09m	09 Sep 2012 00h33m	
Ch2 Length (h)	6.89	5.89	6.89	6.89	
Ch2 $t_{exp}(s)$	12s	12s	12s	12s	
Ch2 N_{exp}	1893	1619	1893	1893	

References. — 1. Geballe et al. (2002), 2. Skrutskie et al. (2006), 3. 2MASS Point Source Catalog, 4. Knapp et al. (2004), 4. Chiu et al. (2006), 5. Zapatero Osorio et al. (2014), 6. Faherty et al. (2012), 7. Reid et al. (2008), 8. McLean et al. (2003), 9. Dahn et al. (2002)

period with the Palomar 60-inch found no variability within their detection limits of 0.09 mag. Subsequent *Ks* band monitoring found no periodic variability over a 2.7 year photometric sampling at their detection limit of 0.04 mag (López Martí and Zapatero Osorio, 2014). Companion searches in wide-fields (2-31″, separations of 101–1,656 AU, brightness limits of $J \sim 20.5$ & $K \sim 18.5$, (Allen et al., 2007) and narrow-fields (HST, $\geq 0.''06$, projected separation (3AU), at Δm_{F814W}=1, Bouy et al. 2003) was also negative. Zapatero Osorio et al. (2014) measured its parallax as 21.2 ± 0.7 mas, resulting in a distance of 47.22 ± 1.56 pc.

3.3 The L5 Dwarf SDSS0107

SDSS0107 was discovered by Geballe et al. (2002) who initially classified it as an L5 based on its optical spectrum. It has been noted as a peculiarly red L dwarf (J–K=1.31), and subsequently categorized with an optical spectral type of L8 (Hawley et al., 2002) and as an L5.5 in the near-infrared by Knapp (2004). An HST/NICMOS search for companions as close as 0.1″ was negative at limits of $m_{110} = 21.9$ mag and $m_{170} = 20.0$ mag (Reid et al., 2006). Its trigonometric parallax was measured by Vrba et al. (2004), resulting in a distance of 15.59 ± 1.10 pc. SDSS0107 has been identified as a member of the Hyades moving group by Jameson et al. (2008), which has an age estimate of 625 ± 50 Myr (Perryman et al., 1998).

3.4 The Young, Low-Gravity L6 Dwarf 2M0103

2M0103 was discovered by Kirkpatrick et al. (2000) and classified with an optical spectral type of L6. Faherty et al. (2012) measured the parallax of 2M0103 at 46.9 ± 7.6 mas, resulting in a distance of 21.90 ± 3.55 pc. Faherty also designated this dwarf to be a low-gravity object, and underluminous in the near-infrared bands compared to the average of its spectral subtype. Gagné et al. (2014) found that 2M0103 was a strong candidate (76.0% probability) to be a 10–11 $M_{\rm Jup}$ *planemo* member of the Argus moving group. A search for planetary-mass companions using HST/NICMOS high-resolution spectral differential imaging was negative (Stumpf

et al., 2010), as was a wide-field search for companions (2–31″, separations of 57–877 AU, brightness limits of J∼20.5 & K∼18.5, Allen et al. 2007). Enoch et al. (2003) reported a possible detection of variability in Palomar 60-inch *Ks*-band observations with a peak-to-peak amplitude of 0.1 ± 0.02 mag over a 29-day period.

3.5 The L3 Radio Emitter 2M0036

2M0036 was discovered by Reid et al. (2000) and identified as an L3.5 by Kirkpatrick et al. (2000) with optical spectra. Knapp et al. (2004) assigned a near-infrared spectral type as $L4 \pm 1$. Dahn et al. (2002) measured its parallax as 114 ± 0.8 mas, corresponding to a distance of 8.80 ± 0.62 pc. A wide field companion search (2–31″, separations of 18–273 AU, brightness limits of J∼20.5 & K∼18.5, Allen et al. 2007), as well as a narrow-field search for companions (HST, $\geq 0''.06$, projected separation (0.5 AU), at Δm_{F814W}=1, Bouy et al. 2003) was negative.

2M0036 is a known broad-band radio emitter (Berger 2002), with coherent and observed unpolarized radio emissions at 4.88 GHz, and an identified period of 3.08 ± 0.05 h (Hallinan et al., 2008). Hallinan concluded that the radio emission is due to cyclotron maser instability, and that the dwarf's axis of rotation is nearly perpendicular to the observed line-of-sight based on previous measurements of $v\sin i$ by Zapatero Osorio et al. (2006) of 36 km s^{-1}. Previously, Lane et al. (2007) reported I-band variability with a period of 3 h, with irregular amplitude. Noting that the radio variability implied a strong magnetic field for 2M0036, Lane postulated that the variability could be due to magnetically induced spots possibly coupled with time-varying features such as dust clouds. Most recently, Blake et al. (2010) measured this dwarf's $v\sin i$ as 35.12 ± 0.57 km s^{-1} and its radial velocity as 32.84 ± 0.17 km s^{-1}.

With its previously known radio variability, 2M0036 was an added WoW target that was not part of the survey's unbiased target selection. Metchev et al. (2015) selected this target for observation as a control for recognizing potential activity-induced photometric effects. In this work, we will investigate its Ch1 and Ch2

variability as the consequence of clouds and thermal perturbations in the same way as our other three dwarfs.

CHAPTER 4

OBSERVATIONS AND DATA REDUCTION

4.1 Observations and Data Reduction

Spitzer observations for our four targets were conducted in 2012; an observing log can be found in Table 3.1. The typical WoW observation lengths for each channel ($\sim$14 h for Ch1, $\sim$7 h for Ch2) were shortened for 2M0036, since its photometric period in other bands had been previously found (Metchev et al., 2015).

All data reduction used the full-frame (256×256 pixels) post-calibration CBCD data products released by the Spitzer Science Center, in addition to each frame's pixel uncertainty values. CBCD flux densities were converted into electrons for photometry and error calculation using the EXPTIME, FLUXCONV and GAIN keywords in the CBCD headers. 2M2208 was placed in the "sweet spot" near the center of the well-characterized sub-array near pixel position [23,231]. 2M0036, SDSS0107, and 2M0103 were placed near [126,130] for Ch1, and [127,128] for Ch2, for purposes of assisting follow-up ground observations. We found no difference in sensitivity, noise, or the ability to correct the pixel phase effect (described below) between the two array positions for a variety of WoW targets that were imaged in both locations. Representative Ch1 frames overlaid with the photometric apertures used are shown in Figure 4.1.

4.2 Corrections for Intrapixel Sensitivity Variations

Spitzer IRAC Ch1 and Ch2 arrays in the warm mission provide flux measurements that are correlated with the array position of the target. The correlated flux measurements are due to intra-pixel sensitivity across each array (e.g., Reach et al. 2005; Charbonneau et al. 2005; Knutson et al. 2008). For time-series photometry, this has

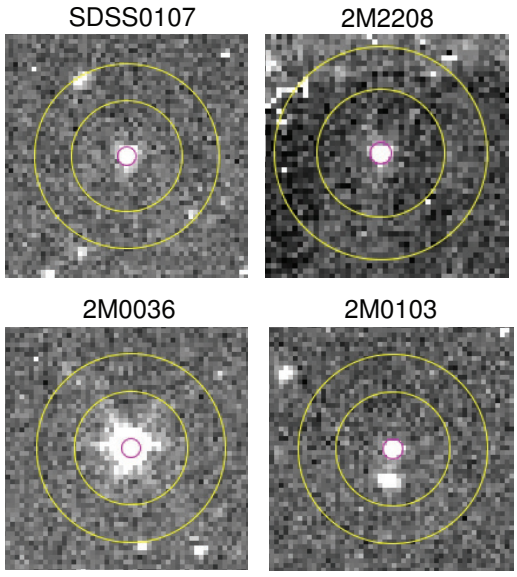

Figure 4.1 Representative Ch1 frames for our four L dwarfs, overlaid with the photometric flux apertures (red) and background annuli (yellow). All non-target sources and bad array elements were masked out of background and flux calculations. Bad array elements near the edges of the Ch1 array for 2M2208 were also masked out.

the effect of a general increase in measured flux as the target centroid moves near the pixel's area of highest sensitivity during the observation, usually near the center of the pixel, and a measured decreased flux as the target moves toward the edges of the pixel. This effect can also be dependent on the intensity of the flux on the pixel.

In addition to the target's x and y position on the pixel, another useful metric that can be used to remove position-correlated changes in the data is the "noise pixel" (NP) (Mighell 2005; Knutson et al. 2012; Lewis et al. 2013), a measure of the width of the stellar point spread function, defined by:

$$\tilde{\beta} = \frac{(\sum_i I_i)^2}{\sum_i I_i^2} \tag{4.1}$$

where I_i is the measured intensity in the i^{th} pixel. We used two separate pixel phase correction methods for each observation, and compared the results against each other. The first method is the result of fitting a quadratic formula fit to the centroid's x and y position within the pixel (e.g., Reach et al. 2005; Knutson et al. 2008) with noise pixel values added in a linear combination to positional information.

Unlike the Spitzer exoplanet transit observations of the latter work, we do not have *a priori* astrophysical reference signals to introduce into the reduction method, as cloud activity can change or mask the brown dwarf's rotational periodic variability on short and long timescales (Artigau et al. 2009; Metchev et al. 2015).

The linear combination of quadratic terms was fit to each observation using a least-squares method, after finding the target's centroid position using IRAC's IDL[1] procedure *box centroider.pro*[2] using a box width of 5 pixels, and calculating the noise pixel values with a circular photometry radius of 4 pixels. The second pixel phase correction method was using "pixel maps" that use low-pass Gaussian spacial filters (Knutson et al. 2012; Lewis et al. 2013), summing the gaussian contributions from the nearest nearest neighbors (NN) in x, y, and noise pixel space. With this method, we performed corrections for a small NN (50) and large NN (400), and had very similar results for all four targets. We chose the 400 NN correction to use for the corrected flux in this work for all of our targets due to their relative brightness enabling reliable flux and position contributions from other neighbors in x,y, and NP space.

Aperture photometry was performed on all eight time series using the IDL procedure *aper.pro*[3] routine to return sky-subtracted flux values for each integration, with sky calculations performed within an annulus centered on each star. The centroid of the target was calculated for each frame using *box centroider.pro*. This position was then used to center the photometry aperture and sky annulus. A range of fixed aperture radii from 2.0 to 3.0 pixels. as well as apertures that varied with noise pixel values (with additive constants ranging from 0-0.5), along with sky annuli ranging [3-15,5-28] pixels were evaluated for scatter in the resulting light curve when corrected for intrapixel phase sensitivity. For both Ch1 and Ch2 observations, a fixed aperture radius of 2.0 pixels and a sky annulus set to an inner and outer radius of [12,20] respectively was chosen to produce low scatter in the resulting time

[1]the acronym IDL represents Interactive Data Language

[2]provided on the *Spitzer* home page: *http://irsa.ipac.caltech.edu*

[3]provided by the IDL Astronomy User's Library at: *http://idlastro.gsfc.nasa.gov*

series photometry. Unrelated stars in the background annulus areas were masked from flux and background level calculations, as was the amplifier glow and bad array elements near the edges of the IRAC arrays. Photometry points with centroid positions outside of 5σ in x or y from a 25-point smoothed median value were rejected, as were sky-subtracted photometry values outside of 5σ. Rejected flux points due to clipping resulted in the rejection of $< 3\%$ of total flux points for each channel run. Each time series was normalized to its own mean value, and binned in 5 minute intervals to reduce noise. Spacecraft pointing stability during all observations was assessed as excellent, with the position drift in x and y limited to < 0.2 pixels in each direction, which resulted in relatively minimal pixel phase correction required.

CHAPTER 5

SPITZER PHOTOMETRY RESULTS

The final light curves for all eight time-series are presented in Figure 5.1, assembled on a timescale relative to the first Ch1 observation of each target. Peak-to-trough variability amplitudes for the four dwarfs in Ch1 range from 0.44–1.80% and from 0.33–1.51% in Ch2. Derived periods range from 2.56 h (2M0036) to 10.16 h (SDSS0107). Uncertainties for the 5 min binned data points range from 0.05% (2M0036, Ch1) to 0.26% (2M0103, Ch2).

Derived periods, peak-to-trough amplitudes and the correlation search values can be found in Table 5.1. In the following subsection, a brief explanation is given for how these values were determined.

5.1 Period Finding and Amplitudes

Period searching was performed in both channels for all four targets using epoch folding of the light curves (e.g., Davies 1990, Leahy et al. 1983, Schwarzenberg-Czerny 1989). Each light curve was folded with a set of trial periods ranging from 1 h to the length of each channel's observation, and a pulse profile was generated. We calculated χ^2 statistics for all trial periods to check for constancy, and the period with the maximum χ^2 (maximum deviation) was taken as the best possible period. We determined uncertainties in the period with 10^5 Monte Carlo simulations, with epoch folding the light curves of each trial with simulated Poisson errors and subsequently computing the standard deviation of the results. Phase-folded light curves to these periods are found in Figure 5.2.

Data from 2M0036 did not phase fold to a particular period in Ch1, and its period in that channel was determined from evaluating a maximum power peak in a Lomb-Scargle periodogram (Scargle 1982), with its uncertainty calculated by the

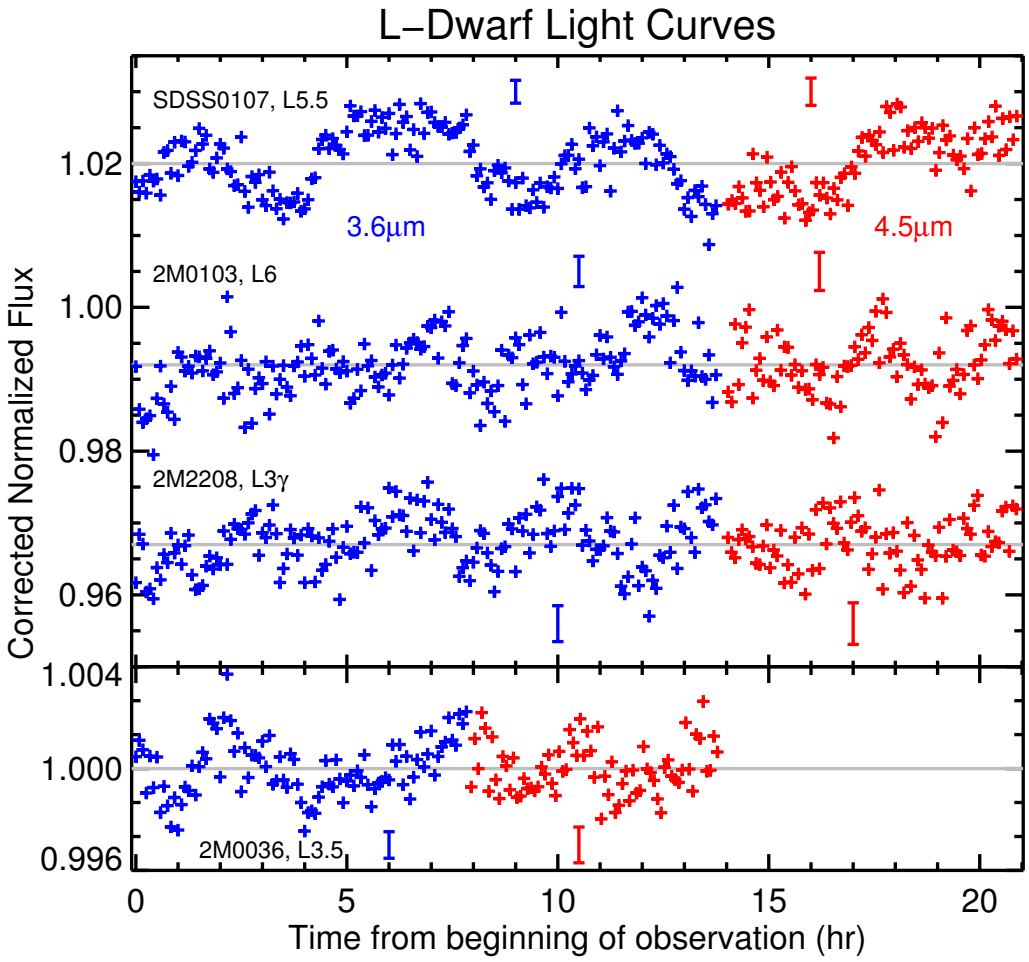

Figure 5.1 Ch1 and Ch2 light curves for all four targets, each plotted with a vertical offset for the purpose of the figure. The grey horizontal lines represent the relative mean flux level for each dwarf. Note that 2M0036 is plotted on a smaller scale for clarity.

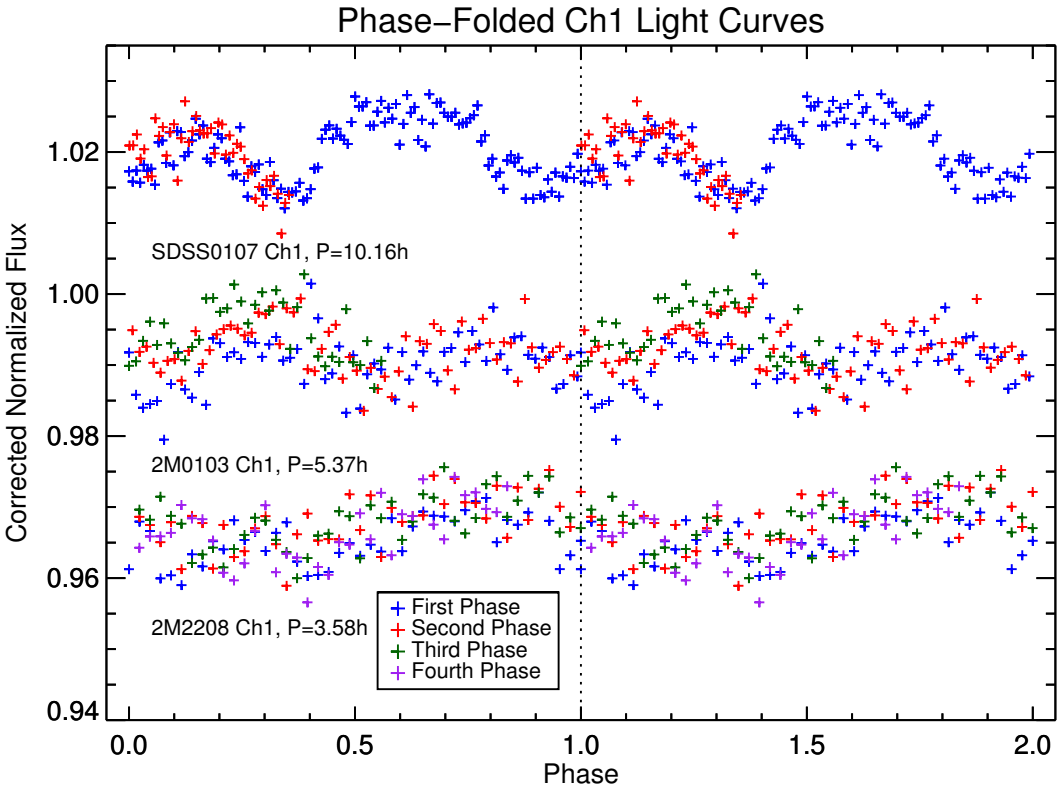

Figure 5.2 The light curves for three of our targets in Ch1 are in good agreement with the period found by epoch-folding (2M0036 does not fold to a particular period in Ch1). Phase-folded Ch1 light curves for the three targets for which a period could be derived from epoch folding are plotted above. The folded phases are plotted twice for clarity, and the respective periods are indicated for each light curve.

Table 5.1. Derived Properties for Targets from Photometry

Quantity	SDSS0107	2M0103	2M2208	2M0036
Relative amplitudes, Ch1 (%)	1.58 ± 0.05	1.78 ± 0.09	1.80 ± 0.09	0.44 ± 0.02
Relative amplitudes, Ch2 (%)	1.51 ± 0.07	1.44 ± 0.09	1.02 ± 0.09	0.33 ± 0.02
Relative amplitude ratios, Ch1/Ch2	1.05 ± 0.06	1.23 ± 0.10	1.77 ± 0.18	1.35 ± 0.10
Periods				
Period, Ch1 (h)	10.16 ± 0.26	5.37 ± 0.56	3.58 ± 0.30	2.63 ± 0.81
Period, Ch2 (h)	*a*	5.78 ± 0.80	3.44 ± 0.42	2.56 ± 0.21
Correlation Lag (deg)[b]	90.50	0	0	0
Absolute Photometry				
Ch1 (mag)	12.34 ± 0.03	12.87 ± 0.03	13.07 ± 0.03	10.26 ± 0.03
Ch2 (mag)	12.17 ± 0.03	12.73 ± 0.03	12.87 ± 0.03	10.25 ± 0.03

Note. — a. No reliable period found in data b. Ch 2 relative to Ch 1

same method as above. 2M0036 Ch2 did phase-fold to a period, which corresponded to the Ch1 period within the uncertainties of both channels.

We calculated maximum relative peak-to-trough amplitudes for all time series from a 60-point ($\sim$ 13.4 minutes) boxcar-smoothed version of the unbinned relative light curve. We calculated the uncertainties in the relative amplitudes by taking the standard deviation of the noise in the smoothed light curve.

5.2 Searching for Correlations and Phase Shifts

Phase shifts in the regular periodic signals between the Ch1 and Ch2 light curves for each target were investigated using a Z-transformed Discrete Correlation Function algorithm (ZDCF, Alexander 1997) to calculate the cross correlation coefficient between the Ch1 and Ch2 binned data for lags (Ch2–Ch1 times) ranging from 1 to 14 hours in 4 minute intervals. We choose this method over standard cross correlation methods to avoid altering the light curves by interpolating them in time; the light curves have significant features that occur on relatively short time scales.

The ZDCF also removes known biases of the standard Discrete Correlation Function (Alexander 1997), and has a method of calculating the uncertainties in any found lag. The lag value with the maximum ZDCF value was taken as the most likely match of the Ch2 data to the Ch1 data. Uncertainties on the best lag as well as the ZDCFs for each lag were calculated by calculating the ZDCFs for 10^3 Monte Carlo simulations. The most significant lags for 2M0103 and 2M2208 corresponded to the length of their respective periods (5.37 and 3.58 h, with ZDCF=0.6 and 0.7, respectively) within the period uncertainties. We therefore conclude that there is no measurable phase shift between Ch1 and Ch2 for these two dwarfs.

SDSS0107 showed a large ZDCF value (0.7) at a lag of -12.96 h between Ch1 and Ch2, with Ch2 being ahead of Ch1 by 0.25 of the derived Ch1 period, or 90.50° if describing this as a phase shift. Upon inspecting the overlap of the Ch1 and Ch2 data when shifted with this lag, it appears that the shape of the Ch2 light curve resembles the shape of the middle peak of the Ch1 data, but with some differences. The dip in the Ch2 plateau at this feature is more pronounced than in Ch1, and the Ch2 feature preceding the maximum appears to be damped when compared to the aligned feature in Ch1. Figure 5.3 plots both channels of data with and without the found lag to illustrate the similarity of the two light curves. While there are some differences, the basic structure between the Ch1 light curve and the shifted Ch2 light curve are similar.

However, SDSS0107 Ch1 observations last slightly longer than the calculated single period, while Ch2 is less than one period in this dataset. Because of this and the differences that do exist between the Ch1 and shifted Ch2 light curves, we do not have enough information to conclusively describe these signals as a periodic signal with a phase shift in Ch2. We conclude that these two correlated features may have some relationship that resembles a phase shift between two periodic signals in our data. Section 6.4.5 describes some of the atmospheric dynamics involved in brown dwarf atmospheres that have been used to explain phase shifts found between other NIR wavelengths in a brown dwarf.

Other possibilities that explain the SDSS0107 light curves include that at the

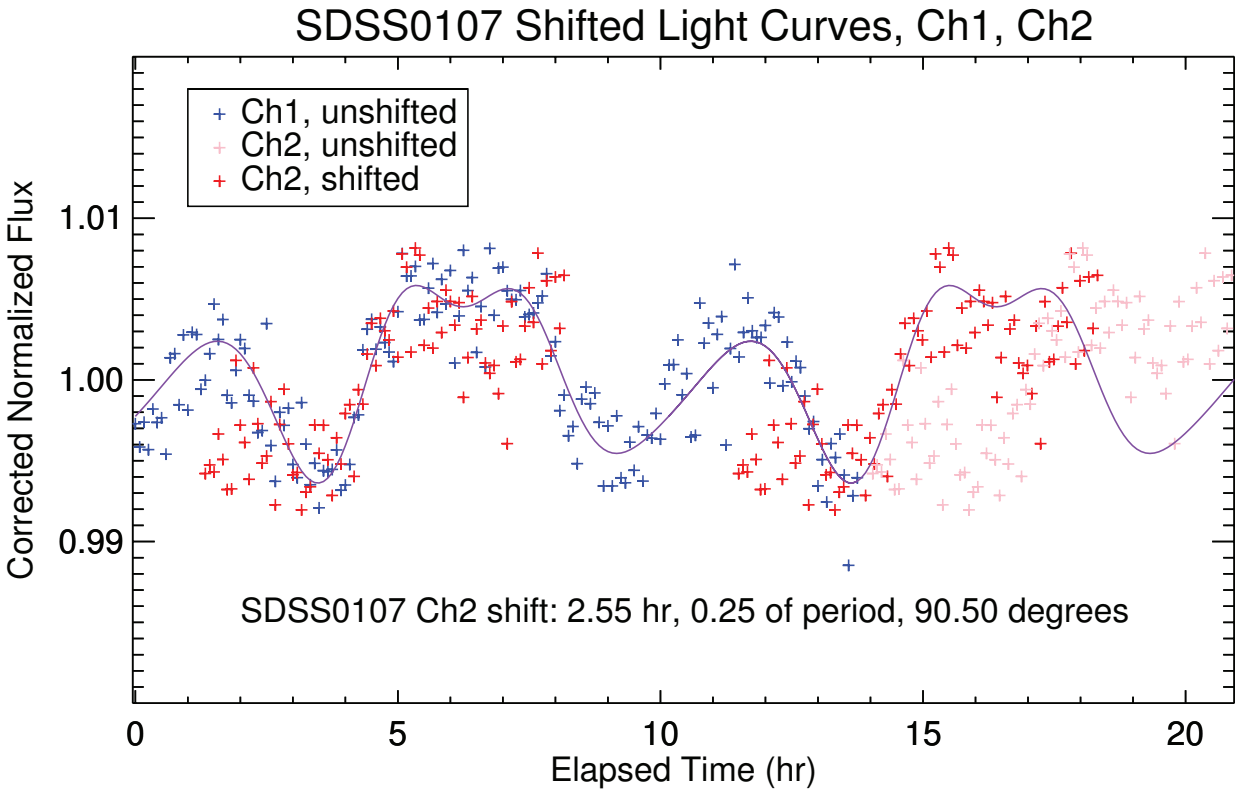

Figure 5.3 A possible correlation between Ch1 and Ch2 light curves in SDSS0107 is plotted, with shifted Ch2 data (red) plotted against Ch1 data (blue). The shift in time for Ch2 was calculated by lag values corresponding to a maximum ZDCF (correlation) value. Red points represent Ch2 data with an applied shift, plotted both with one value of shift and values of period+shift to overlap with Ch1 data. The continuous curve is a 5-term Fourier fit to Ch1 data showing how the shifted features lines up when two phases of Ch1 are plotted. Light red points are original Ch2 data without the shift in time.

moment when the Ch1 observation was ending and the Ch2 observation began, the dwarf began undergoing activity that masked its regular periodicity, or that the light curve of SDSSS0107 is quite complex, with the period of SDSS0107 actually much longer than 10.2 h (the folding we find being coincidental), and that we have not observed its true period after 13 h of continuous observations. We note that a full period measurement in Ch2 would provide invaluable evidence for any phase shift between these two channels.

5.3 Absolute Photometry

Absolute photometry was performed on all eight time series using the procedures of Reach et al. (2005). For each integrated CBCD frame, we used the centroid positions and noise pixel values found with the procedures described in the previous section, with a fixed photometric aperture with a radius of 2 pixels and a background annulus of [12,20]. We also applied array location-based and aperture corrections from Reach et al. (2005), and pixel phase correction was performed as above. The resulting photometry was then medianed over the length of the time series, and converted to magnitudes using the zero-flux points of 280.9 and 179.7 Jy for Ch1 and Ch2 respectively. The results from the photometry can be found in Table 5.1.

Color-magnitude diagrams were generated for the four L dwarfs using the derived absolute photometry and distance moduli from the parallaxes in Table 3.1. Figure 5.4 shows the Spitzer color-magnitude diagram for these objects plotted with L and T field dwarfs that have both measured Spitzer fluxes and parallaxes compiled by Dupuy and Liu (2012). The low-gravity L3 dwarf 2M2208 has an $M_{[4.5]}$ brightness similar to the L5 dwarf SDSS0107, but a brightness even lower than the low-gravity L6 dwarf 2M0103. Also plotted is a color-magnitude diagram of previously measured *JHK* magnitudes compiled in Table 3.1, plotted similarly with field dwarfs with known parallaxes from Dupuy and Liu.

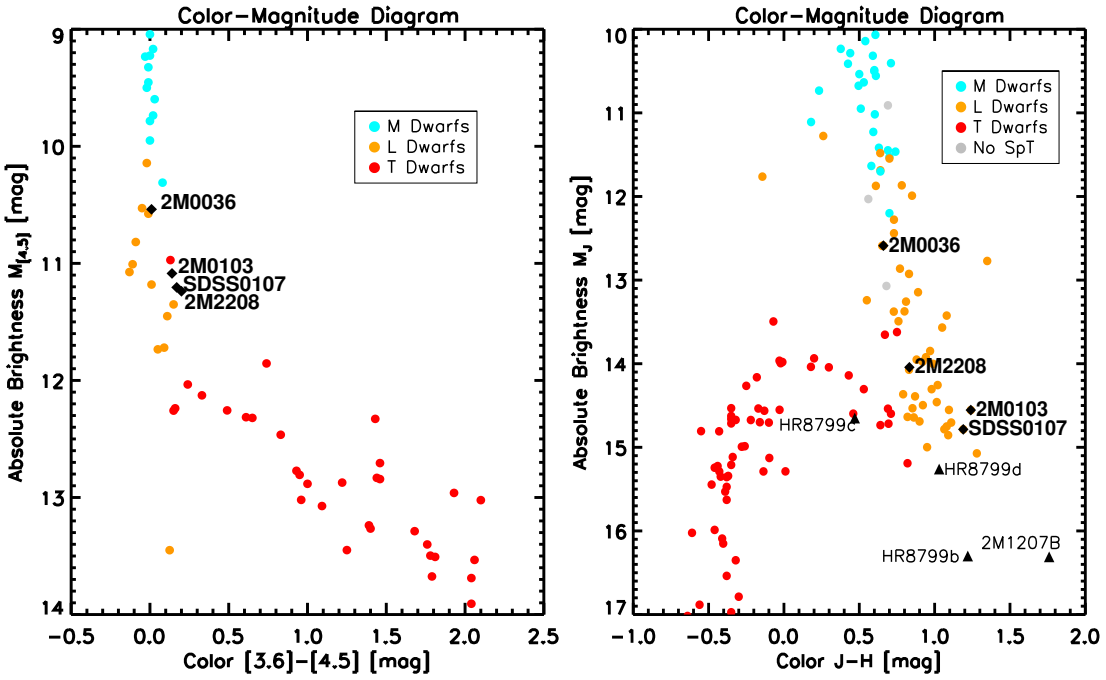

Figure 5.4 Left: Color magnitude diagram in Spitzer Ch1 and Ch2 using time-medianed photometry from this work for the four target dwarfs, with a selection of M, L and T field dwarfs shown with parallaxes from Dupuy and Liu (2012). The low-gravity L3γ dwarf 2M2208 has an $M_{[4.5]}$ brightness similar to the L5 dwarf SDSS0107, but a brightness even lower than the low-gravity L6 dwarf 2M0103. Right: Color-magnitude diagram in J and H bands, from compiled literature magnitudes for our targets, HR8799 planets, and 2M1207b. 2M0103 and SDSS0107 are extremely red L dwarfs with colors comparable to the HR8799 planets.

5.4 Discussion

All four L dwarfs are clearly variable in both Spitzer channels, with distinct light curve shapes. The light curve of 2M0036 has an irregular shape in Ch1, but a more regular pattern in Ch2. The relative brightness of 2M0036 allows the robust detection of its low amplitude of 0.33% in Ch1, representing the lowest amplitude of our targets, with the highest amplitude being detected in the low-gravity L3γ dwarf 2M2208 at 1.80%, also in Ch1. All targets have similar amplitudes in both channels, but with marked light curve differences in each case. The amplitudes in both channels for each object are similar, with a maximum Ch1/Ch2 amplitude ratio of 1.77 (2M2208). The periods of these L dwarfs range from 2.56 ± 0.21 h for 2M0036, to 10.16 ± 0.26 h for SDSS0107. The light curves of SDSS0107 and 2M0103 show distinctive double-peaks.

5.4.1 Light Curve Evolution

Light curve evolution (LCE) is the change in light curves shape and characteristics over time. One way to characterize LCE is to subtract the light curve of the first cycle (the "reference" cycle) from subsequent cycles. We did this for each object by taking the phase-folded light curves of binned data from Figure 5.2, and interpolating each subsequent phase to the phase values of the reference cycle data. We used quadratic interpolation for this purpose, although linear and spline interpolations gave similar results. The residuals obtained after subtracting the reference cycle light curve are shown in Figure 5.5. The long period of SDSS0107 ($\sim$10.2 h) makes it difficult to characterize any evolution in the incomplete second cycle of the light curve, but a discussion on the evolution of 2M2208 and 2M0103 follows.

2M0103

Figure 5.5 shows changes in the light curve from the first period to be as high as $\sim$2%. A major evolution feature that can be seen in this LCE plot is the general brightening of the source after the first period. We investigated if this brightening

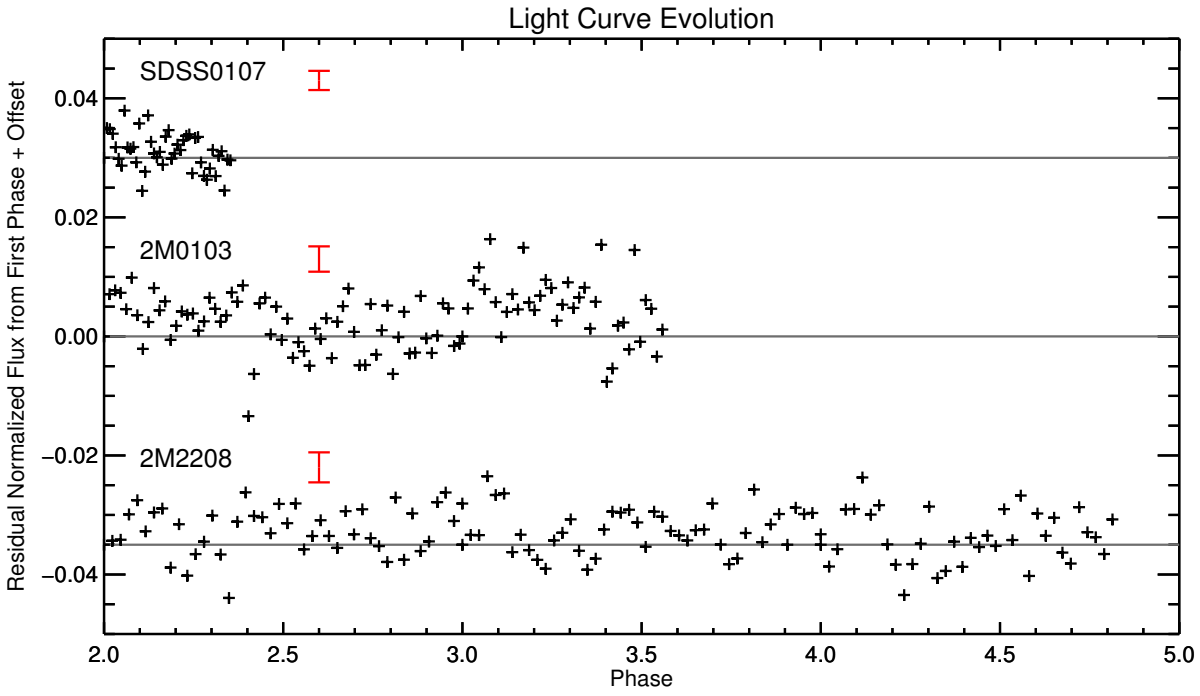

Figure 5.5 Light curve evolution of the three photometrically periodic targets in Ch1 that epoch-folded to a period show changes from the first phase between 0–2%, with a general brightening trend in Ch1 of 2M0103 of ∼0.5%. For each target, the phase-folded light curve was subtracted from the first phase after each subsequent phase was interpolated to the same time-grid in phase space as the first. A medianed noise level for the subtracted phases is shown in red for each dwarf.

was due to uncorrected pixel phase effect, as the source is moving toward the center of the IRAC pixel it was placed on during this observation. Such a movement could result in increased flux values over time as the sensitivity of the pixel is generally higher in the center of each pixel. Photometry for this object was repeated at a series of shorter time intervals for this Ch1 time series, correcting pixel phase effects with both noise-pixel and quadratic function-fitting to centroid positions. Evaluating shorter intervals should allow for the more efficient correction of any brightness ramp due to pixel phase effect, i.e. a better fitting to noise-pixel maps and x-y space for any correlation of position and flux when the ramp is small. However, the brightening feature remains in all smaller time-interval photometry reduction and pixel phase effect correction, including those intervals for which there is no net movement of the pixel over the array. We suggest that this brightening is physical, and not due to intrapixel movement of the source on the array.

2M2208

This dwarf shows more modest light curve evolution nearer the noise level of the light curves, although we can see instances of evolution from the reference period of $\sim 1\%$ that are sustained for less than half a period.

CHAPTER 6

MODELING AND SPECTRAL FITTING

In this chapter, we describe our efforts to use one-dimensional spectral models to match a mean model spectrum to each dwarf, determining best-matched T_{eff}, $\log g$, and cloud parameters used in further investigations in this work. We will first describe the details of the models, followed by a description of the method used in determining the best-matched mean model spectra to observed archived NIR spectra. Finally, we will present the results of these matches for our four dwarfs.

6.1 Description of the Models

To evaluate possible physical mechanisms of periodic photometric variability as well as any light curve evolution, we will consider the complex structure of clouds at different pressures and temperatures in a given brown dwarf atmosphere. Using principal component analysis, Apai et al. (2013) showed that for two L/T transition dwarfs, over 99% of the observed periodic photometric variability can be reproduced with the linear combination of just two different spectra, concluding that all of the features in the visible photosphere share the same spectra. In that study, variations in cloud thickness were found to account for the dwarfs' periodic photometric variability. Buenzli et al. (2013, 2015a,b) performed a detailed fit to the spectra of L/T variables and found that the varying NIR spectra of those dwarfs are well fit by the linear combination of two models that differ in T_{eff} and cloud opacity parameters.

In this perspective, we will first find global atmospheric parameters for each of our four dwarfs by fitting NIR spectra and the median observed Spitzer fluxes from this work with one-dimensional cloudy atmosphere models. The fitted models then serve as reference for the subsequent analysis of the Spitzer light curves.

The atmosphere models used here are described in Saumon and Marley (2008).

These brown dwarf atmospheric models give temperature-pressure structures in radiative/convective equilibrium and the corresponding synthetic spectra. The thermal radiative transfer is modeled with the source function method of Toon et al. (1989) and allows the inclusion of arbitrary Mie scattering particles in the opacity of each layer. All models used here use the solar elemental abundances of Lodders (2003) and the opacity database is described in Freedman et al. (2014). Our baseline cloud model (Ackerman and Marley, 2001) parametrizes the efficiency of sedimentation of cloud particles through an efficiency factor, $f_{\rm sed}$. Large values of $f_{\rm sed}$ correspond to rapid particle growth and large mean particle sizes. In this case, condensates quickly settle, leading to physically and optically thin clouds. When $f_{\rm sed}$ is small, particles grow more slowly and the atmospheric condensate load is larger and clouds thicker. The cloud model is fully coupled with the radiative transfer and self-consistent with the (P, T) structure of the model. Finally, the models consider non-equilibrium chemistry driven by rapid vertical mixing, a process that has been found to be prevalent in brown dwarf atmospheres (Griffith and Yelle, 1999; Saumon et al., 2006; Stephens et al., 2009). Its main effect in late L dwarfs is to reduce the atmospheric abundance of CH_4 in favor of an increased fraction of CO. The mixing time scale in the convective region is obtained from the mixing length theory and it is parametrized by the coefficient of eddy diffusion K_{zz} in the overlying radiative zone. We chose a value of $\log K_{zz}(\mathrm{cm}^2\,\mathrm{s}^{-1}) = 4$, which is representative of the values found in previous studies. The Saumon and Marley atmosphere models have been very successful when applied to brown dwarfs and Jupiter (Ackerman and Marley 2001; Knapp et al. 2004; Golimowski et al. 2004; Saumon et al. 2006; Leggett et al. 2007; Cushing et al. 2008; Stephens et al. 2009).

6.2 Model Fitting

We utilized spectra obtained with SpeX spectrograph (Rayner et al., 2003) at the NASA InfraRed Telescope Facility (IRTF), with a spectral range of 0.6–2.6 μm, initially downloaded from the SpeX Prism Spectral Library for SDSS0107, 2M0103,

and 2M0036 (Burgasser et al. 2010; Cruz et al. 2004; Burgasser et al. 2008). Unnormalized versions of these spectra were also obtained (Burgasser, A., private correspondence), and were used throughout this work. A SpeX spectrum for 2M2208 (Cruz et al., in prep) is presented for the first time in this work. The observing log for these spectra can be found in Table 6.1.

We noted that the JHK flux values for the spectra for 2M0036, 2M0103 and SDSS0107 did not match literature 2MASS JHK flux values calculated from the values found in Table 3.1; 2M0036 in particular deviated from these values by more than a factor of 8. Such proper calibration is necessary to properly fit relative values between the SpeX spectra, spectral models and the model and observed Spitzer fluxes. We adjusted each of these spectra by multiplying data from the spectra by a factor that was calculated from $F_{\lambda,2MASS}/F_{\lambda}$, where $F_{\lambda,2MASS}$ is the flux from literature 2MASS magnitude values at the respective effective wavelength, and F_{λ} is the flux from the SpeX spectra at the effective wavelength of the 2MASS fluxes. These factors were calculated for the 2MASS H and K bands, and a weighted average of the two factors was taken using the SpeX and 2MASS uncertainty values at both respective effective wavelengths. This weighted average was the factor used to multiply the flux values in each spectrum.

Each corrected, reduced spectrum was normalized to a flux value calculated from integrating the flux density of each spectrum from 1.50–1.80 μm; the same value was also used to normalize corresponding observed [3.6] and [4.5] flux values. Model spectra and model Ch1 and Ch2 flux values were normalized together in the same manner.

Each spectra and Spitzer flux pair was matched to a grid of model spectra. The grid of model spectra ranged from T_{eff}=1,200–2,400 K in 100 K steps, $\log g(\mathrm{cm\,s^{-2}})$=4–5.5 in steps of 0.5. Cloudy models with f_{sed}=$\{1,2,3,4\}$ as well as models with no clouds (nc) were considered. The parameter space covered in this grid of models was not complete, especially for models in the low gravity ($\log g$=4.0) regime. The models that were available are noted in the final results of this section in Figures 6.4 and 6.5.

Table 6.1. SpeX Observing Log

	SDSS0107	2M0103	2M2208	2M0036
Date	12 Oct 2007	19 Sep 2003	14 Dec 2007	7 Sep 2004
R	120	120	120	120
Reference	Burgasser et al. (2010)	Cruz et al. (2004)	Cruz et al. (in prep.)	Burgasser et al. (2008)

For each model spectra and Spitzer flux pair set, a goodness of fit statistic was calculated between each model spectra, k, and the SpeX spectra based on the procedure of Cushing et al. (2008),

$$G_k = \frac{1}{n}\sum_{i=1}^{n} w_i \left(\frac{f_i - D_k F_{k,i}}{\sigma_i}\right)^2, \tag{6.1}$$

where n is the number of data points; w_i is the weight of ith wavelength and is given by the length of the wavelength bin $w_i = \Delta\lambda_i$, and whose total is normalized to unity; f and F_k are the flux densities of the SpeX and model spectra respectively; σ_i is the noise in the observed flux densities, and D_k is an unknown multiplicative constant for each model that is equivalent to $(R/d)^2$, where R is the radius of the dwarf and d is its distance. D_k is calculated by minimizing G_k with respect to C_k and is calculated by

$$D_k = \frac{\sum w_i f_i F_{k,i}/\sigma_i^2}{\sum w_i F_{k,i}^2/\sigma_i^2}. \tag{6.2}$$

G values can be large due to small uncertainties (bright targets like 2M0036), and will also tend to be dominated by the fit of the Spitzer fluxes over the fit of the SpeX spectra, due to the relatively wide spectral windows in the [3.6] and [4.5] integrations. The challenges of calculating a goodness-of-fit statistic that does not follow these extremes when fitting spectra and photometry has been the subject of much discussion and ongoing experimentation (e.g., Cushing et al. 2008).

For SDSS0107 and 2M2208, the lowest G value was taken as the best-matched model; when visually inspecting the matches resulting from the lowest five G values,

Table 6.2. Best-Fit Dwarf Parameters from SpeX Spectra and Spitzer Flux Matches

	SDSS0107	2M0103	2M2208	2M0036
T_{eff} (K)	1,300	1,400	1,400	1,700
log g	4.0	4.0	4.0	4.5
$f_{\rm sed}$	1	1	1	1

these spectral matches produced good fits to the 1.3, 1.7, and 2.2 μm features in the SpeX spectrum as well as the two Spitzer photometric points. Both of these dwarfs matched models well with similar temperatures, and the same $f_{\rm sed}$=1, and low gravity (log g=4.0), although such low gravity for 2M0103 is lower than its previous designation as a moderately low-gravity object (Faherty et al., 2012). This best-fit low gravity model is consistent with the previous "γ" classification of 2M2208 (Cruz et al., 2009). According to the evolutionary models of Saumon and Marley (2008), this best-fit model also supports the seemingly low best-fit parameter of $T_{eff} = 1,400$ K for this L3γ dwarf. The models calculate an age of $\sim$10 Myr, while also indicating a mass of $\sim$8 $M_{\rm Jup}$, which are values generally consistent with findings from Gagné et al. (2014) and Cruz et al. (2009).

6.3 Heterogenous Clouds as a Cause of Photometric Periodic Variability

In this section, we detail our efforts to evaluate heterogenous clouds as a source of the observed periodic photometric variability in our four L dwarfs. We will first describe the 1-D spectral models we will use to compute Spitzer Ch1 and Ch2 fluxes, and the effects of different model parameters on those fluxes. We then introduce a linear parameterization between two models of cloudy surfaces. Using the best-fit mean spectrum found for each dwarf in the previous section, we investigate what second cloud model has to be fit to best describe the observed Ch1 and Ch2 periodic photometric amplitudes for those dwarfs.

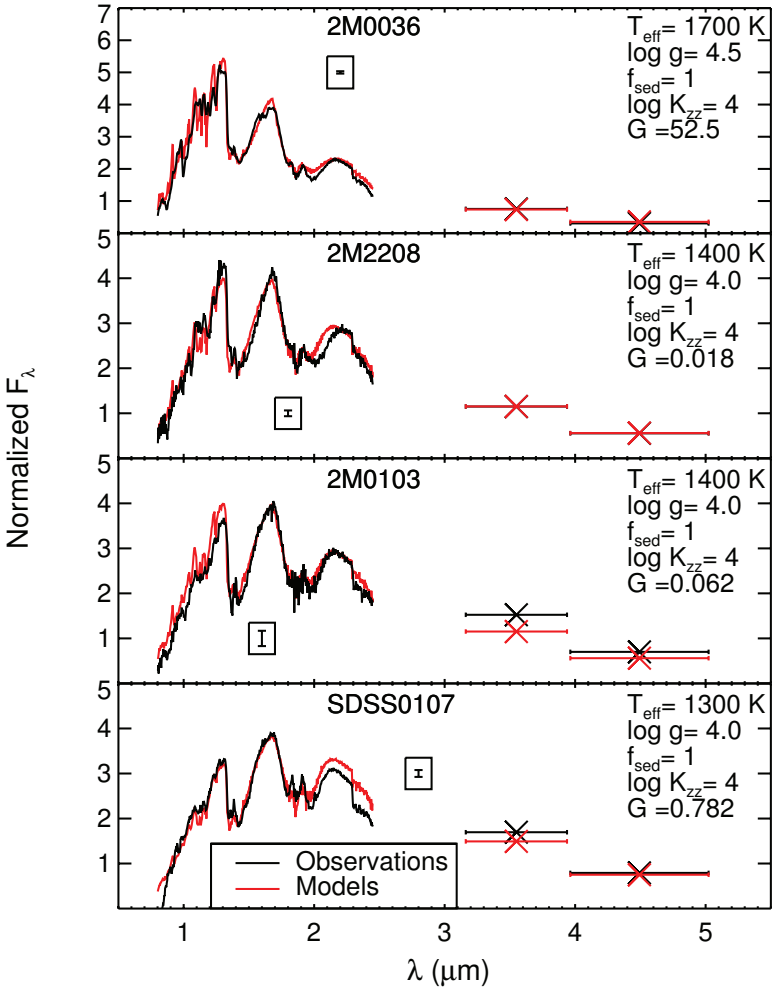

Figure 6.1 SpeX and [3.6] and [4.5] fluxes match well with spectral and flux models for all four dwarfs. Each dwarf's SpeX spectra and observed Spitzer fluxes (black) are plotted with its best-matching mean spectral and flux models (red), with corresponding G values noted. A median noise value for each SpeX observation is plotted in an inset; the error bars in the observed Spitzer fluxes are within the plotted symbols. The T_{eff}, $f_{\rm sed}$ and log g of the best-fit model for each dwarf are noted; all dwarfs matched models with a $f_{\rm sed}$=1.

6.3.1 Description of the Models

The Ackerman and Marley (2001) cloud model successfully reproduces the observed NIR color of L dwarfs. The dramatic shift in the NIR colors through the L/T transition is widely understood as due to a reduction of the cloud opacity as T_{eff} decreases. At the cool end of the transition, the NIR colors of mid-T dwarfs are well explained by cloudless models. The transition can be reproduced in the context of the Ackerman & Marley cloud model with an increase in the $f_{\rm sed}$ parameter (i.e. the cloud particle size, Saumon and Marley, 2008), or alternatively by a decrease in fractional cloud cover (Marley et al., 2010). These results suggest that horizontal variations in cloud properties, modeled by variations in $f_{\rm sed}$ across the surface of the brown dwarf, can produce model flux differences that are realistic enough to be compared to the observed photometric variability amplitudes. For a given T_{eff} and $\log g$, increasing $f_{\rm sed}$ decreases the cloud opacity, resulting in larger Ch1 and Ch2 fluxes, with the Ch1$-$Ch2 color becoming bluer, and vice-versa for increases in $f_{\rm sed}$.

In addition to $f_{\rm sed}$, we also consider variations in the coefficient of eddy diffusion K_{zz} as it affects the chemistry of carbon in L dwarfs and the abundances of two important absorbers: CO and CH_4. Vertical mixing in L dwarf atmospheres tends to increase the mole fraction of CO and the expense of that of CH_4 as these two molecules contain nearly all the carbon available in the atmosphere. The very strong 3.3 μm band of CH_4 falls within the IRAC Ch1 bandpass and the 4.5 μm band of CO is centered on the Ch2 bandpass. The deviation of the CO/CH_4 ratio from chemical equilibrium caused by vertical transport dramatically increases the Ch1 flux for T_{eff} less than approximately 1,500 K, but the models predict a minimal decrease in the Ch2 flux. Thus, increasing K_{zz} makes the Ch1$-$Ch2 color bluer.

The results of Apai et al. (2013) suggest that our Spitzer light curves can be modeled with a rotating brown dwarf that has longitudinal variations in cloud structure described by areas corresponding to two different values of $f_{\rm sed}$. We express the two extremes of the cloud surfaces as

$$F_{combined} = C_1 F_1 + C_2 F_2 \tag{6.3}$$

where F_1 represents a rotational-phase dependent model flux from the best-matched spectrum which we will consider the primary atmospheric component, and F_2 is the flux from a secondary atmosphere component, which is a model with the same $\log g$ but different cloud parameters, and can be thought of as a perturbation of F_1. The contribution from each surface to the combined flux, $F_{combined}$, is parameterized by a C_i, which is a surface area covering fraction, or the surface area covered by a photosphere with a given spectrum divided by the complete surface area of the object. C_2 is the surface area covering fraction of the secondary atmospheric component (e.g., Marley et al. 2010; Apai et al. 2013), while $C_1 = 1 - C_2$ is the surface area covering fraction of the primary atmospheric component.

Our most important assumption in this model is that $C_2 \ll C_1$. This sets the expectation that the overall spectrum of the object is very similar to the spectrum from the F_1 surface, thereby allowing us to treat F_2 as a perturbation. We expect C_2 to be less than approximately 0.1, if we expect this model to match the relatively small variability observed in our dwarfs in Spitzer Ch1 and Ch2. In addition, we assume that we are not observing the dwarf pole-on, as such a viewing geometry would not result in rotationally-modulated periodic photometric variability with persistent atmospheric features in the atmosphere. We additionally assume that the distribution of the surface associated with F_2 is not axisymmetric over the surface of the dwarf, which could also lead to no rotationally-induced variability as no net flux differences would be observed as the dwarf rotates these features into and out of view.

6.3.2 Comparing Model Flux Differences with Observed Amplitudes

We attempted to reproduce the Ch1 and Ch2 amplitudes of the photometric periodic variations (Ch1–Ch2 color changes) in each of our four targets by describing them as a linear combination of fluxes from two model atmospheres. The first model in

this pair (henceforth "base model") is the best-fit to the SpeX NIR spectrum and Spitzer fluxes as described above, while the second model is a model that results in amplitudes from flux differences with the first model that reproduces the closest values to the observed Ch1 and Ch2 amplitudes.

We utilized the model Ch1 and Ch2 fluxes from a similar model grid as the previous fit to spectra and photometry. The best-fit values of Ch1 and Ch2 fluxes found in the previous section were used, and designated as the base fluxes. To search for a best secondary model, a grid of model flux values was utilized that spanned the parameter space of T_{eff}=900–2,400 K in 100 K steps, $f_{\rm sed}$={1,2,3,4,nc (no clouds)}, but we also now consider a range of K_{zz} values that include $\log K_{zz}(\mathrm{cm^2\,s^{-1}})$={2,4,6} as well as equilibrium models with K_{zz}=0. The $\log g$ values for this model grid were the kept the same as found from the base model fitting. The parameter space covered in this grid of models was not complete, especially for models in the low gravity ($\log g$=4.0) regime.

Eliminating Unphysical Secondary Model Possibilities and Limitations of Models

When considering the best secondary model that would reproduce the observed Spitzer amplitudes in our light curves, we must also consider the physical likelihood of a particular secondary model's atmospheric parameters residing in an atmospheric column adjacent to a surface with the parameters with the base model. 1D Temperature-pressure (T-P) profiles are not expected to be extremely different for two different cloud types in these adjacent columns. Marley et al. (2010) modeled two adjacent atmospheric columns of different clouds parameterized with a cloudy contribution fraction into a single consistent T-P profile. However, such an approach is more appropriate for partly-cloudy dwarfs, not for a homogeneous cloud cover with few patches of different cloud parameters, such is our approach here. A more realistic comprehensive model for assuring the physicality of adjacent cloud models would take into account the global circulation of the atmosphere and its dynamics. This intrinsically 3D approach is far more complicated than our 1D

static approach in this work, and while there is progress toward realistic circulation models of brown dwarfs (Showman and Kaspi 2013; Zhang and Showman 2014), future work remains on unifying dynamical and cloud models with respect to observed photometric variability.

Comparing T-P profiles of our models for determining possible physical compatibility is beyond scope of this work; we do not have a meaningful metric for comparing the true likelihood of their physical compatibility in adjacent atmospheric columns. But we will make one basic assumptions about the likelihood of our model pairs residing near each other in an atmosphere for a given set of model parameters. When cloud opacity decreases from our base model to an adjacent secondary model, we would generally expect the T_{eff} of the secondary model to increase, as the reduced opacity allows radiation from deeper levels in the atmosphere where temperatures are warmer. Such a process is seen on Jupiter and its "hot spots" as observed at 5 μm, which have among the lowest cloud opacity anywhere on Jupiter, but also the highest flux in the 5 μm spectral window of anywhere on the planet (e.g., Westphal 1969; Bjoraker et al. 1986; Carlson et al. 1994; Atreya et al. 1999; Showman and Dowling 2000). Therefore, we exclude any secondary models that have an equal or lower T_{eff} and a higher $f_{\rm sed}$ than the base model of each dwarf.

6.3.3 Calculating Model Amplitudes

With the exception of the models we deem unphysical, this model grid was then evaluated for each change in T_{eff}, $f_{\rm sed}$ and K_{zz} whose associated fluxes, when differenced from the base fluxes, created Ch1 and Ch2 model amplitudes according to the equations

$$A_{Ch1,model} = 100 \times (F2_{Ch1} - F1_{Ch1})/F1_{Ch1} \tag{6.4}$$

$$A_{Ch2,model} = 100 \times (F2_{Ch2} - F1_{Ch2})/F1_{Ch2} \tag{6.5}$$

where $F1$ and $F2$ are the channel specific fluxes from Equation 6.3, representing the primary and secondary model fluxes (respectively) that are being evaluated, and $A_{Ch1,model}$ and $A_{Ch2,model}$ are the resulting Ch1 and Ch2 model amplitudes,

respectively, expressed as a relative percentage that can be compared to the observed amplitude values listed in Table 5.1.

With model amplitudes calculated, we investigated which secondary model, when combined with the base model, is the most likely to reproduce the observed amplitudes in both channels. A key factor in evaluating how close the calculated model amplitudes are to our observed amplitudes is determining C_2, the secondary surface area covering fraction that determines the contribution fractions between the base and secondary model fluxes.

For each model amplitude, we interpolated a line in A_{Ch1} and A_{Ch2} space that extends from each calculated amplitude to the origin. A representative example is found in Figure 6.2. This line parameterizes the calculated amplitudes with C_2, the secondary surface area covering fraction, where the slope of the line is $A_{Ch2,model}/A_{Ch1,model}$. The amplitude values (black diamonds) at the top of each line represent C_2=0.5, the amplitude that results from an equal contribution from both model fluxes $F1$ and $F2$. Model amplitudes at the origin are zero, representing C_2=0 (model amplitudes here are calculated only from 100% of the $F1$ (base model) fluxes, 0% of the $F2$ (secondary model) fluxes, and thus no model amplitude results). Points on each line represent values of C_2, and have their own value in A_{Ch1} and A_{Ch2} space. Our dwarfs' observed amplitudes are $\leq 1.8\%$, and in this model amplitude space, reside very near the origin of each dwarf's Figure 6.2 equivalent.

Figure 6.3 shows a detailed region of the respective Figure 6.2 equivalent for each dwarf, but scaled near the observed amplitudes values for each object. In this region, the observed amplitude values are far out of the plot's boundary, with only the C_2 line associated with each amplitude visible. The secondary model parameters associated with each line are labeled. In Figure 6.3, all amplitude values are scaled in units of the uncertainties of the observed Spitzer light curve amplitudes to evaluate the significance of any matches to observations, and the 1σ boundary is plotted as a dashed circle. For clarity, the plots for 2M2208, 2M0036 and 2M0103 are scaled well inside the 1σ circle to show only the closest secondary model matches.

Each interpolated C_2 line was evaluated for its closest approach to the observed

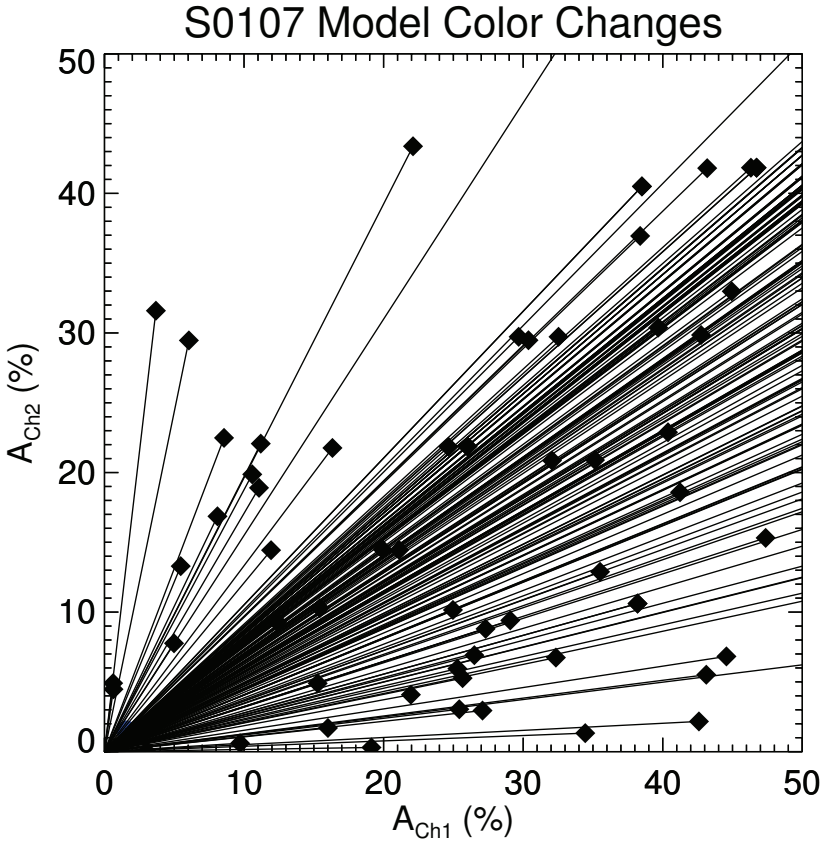

Figure 6.2 A representative plot for one dwarf of the model amplitudes calculated from our model grid using Equations 6.4 and 6.5. A line is interpolated from each model amplitude to the origin, representing values of C_2 from 0.5 to 0, respectively. In this model amplitude space, the observed amplitude of the dwarf lies near the origin.

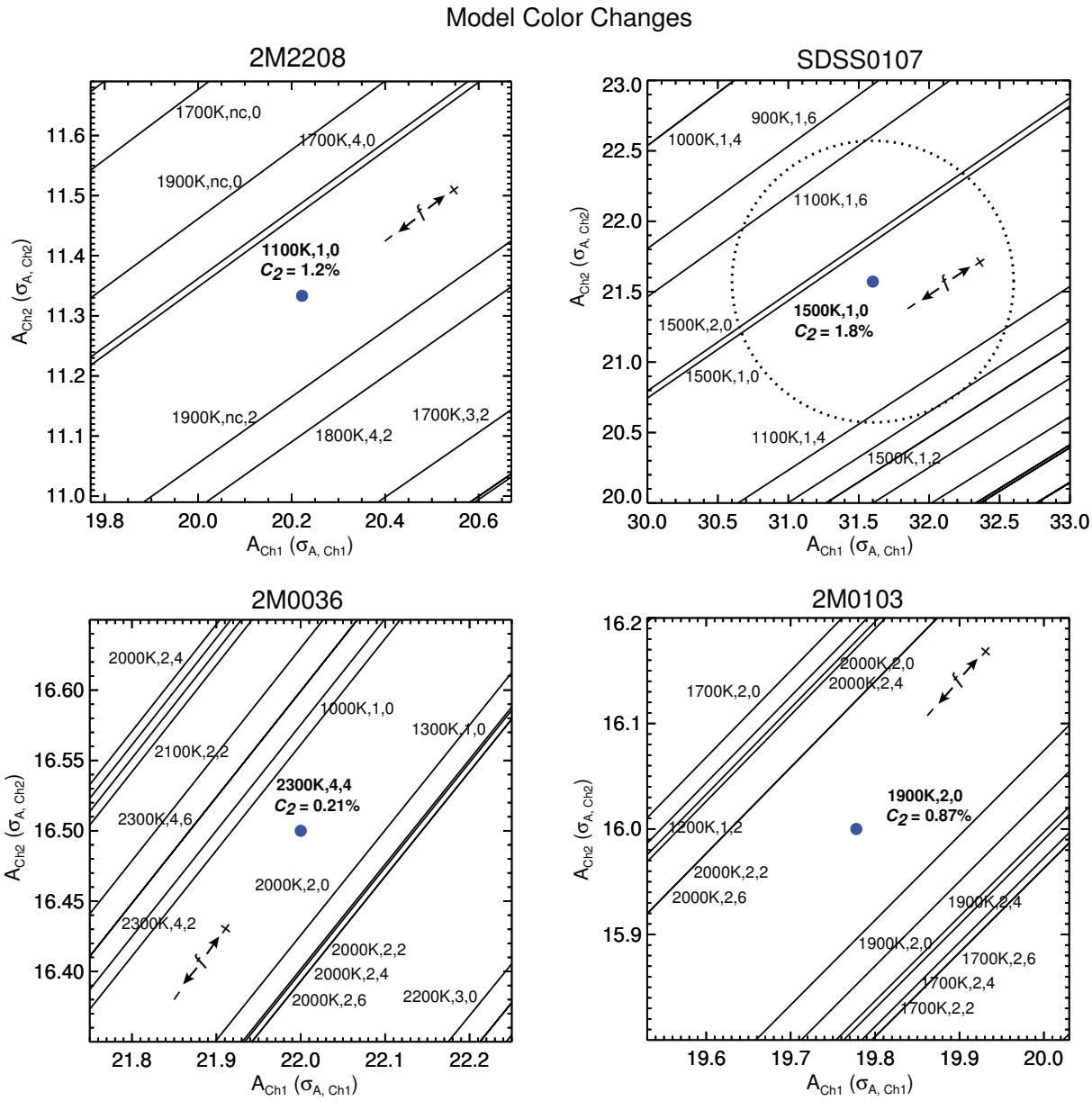

Figure 6.3 Observed Ch1 and Ch2 color changes for all four L dwarfs as described as model Spitzer amplitudes calculated from cloud model pairs parameterized by a secondary surface covering fraction C_2. Secondary models are noted by T_{eff},$f_{\rm sed}$, log K_{zz} parameters. Amplitude values have been scaled in units of the uncertainty of the observed Ch1 and Ch2 amplitudes for each dwarf, and the observed amplitudes from the dwarf's light curve (blue circle) are shown. Each model amplitude value is parameterized by a line of C_2 values from C_2=0 (the origin) to 0.5 (calculated model amplitude) as described in the text. The best-matched secondary model to the observed amplitudes are in bold. The 1σ uncertainty value is depicted as the dashed circle, and we consider all models within this circle also likely matches. This circle is outside the plot for 2M2208, 2M0036 and 2M0103.

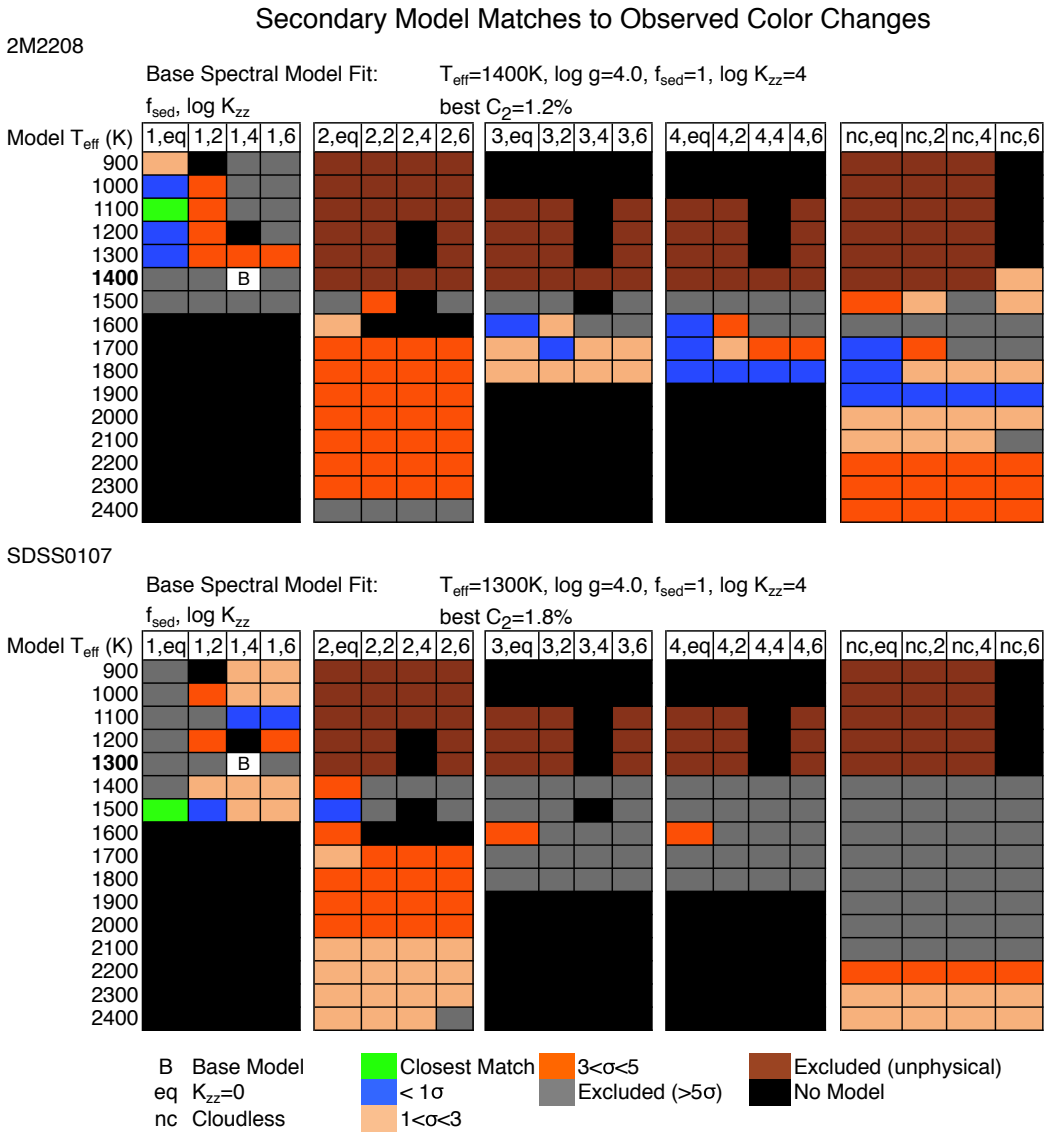

Figure 6.4 Model pair combinations reproduce the observed Ch1–Ch2 color changes for 2M2208 and SDSS0107. The parameter space is grouped by $f_{\rm sed}$={1,2,3,4,nc (no clouds)}, and may be best visualized as existing in 3D stacked on top of each other in this order. B is the base model determined from spectra and flux matching, and green shows the single best matching secondary model that reproduces the observed color change for each dwarf, with the corresponding secondary surface area covering fraction C_2 noted. Other matches within 1σ are in blue, while secondary models we exclude ($> 5\sigma$) or that are likely unphysical (see text) are in grey and brown, respectively. Models within 1σ are constrained in T_{eff} to $\pm 200K$ for SDSS0107 and $^{+500K}_{-400K}$ for 2M2208.

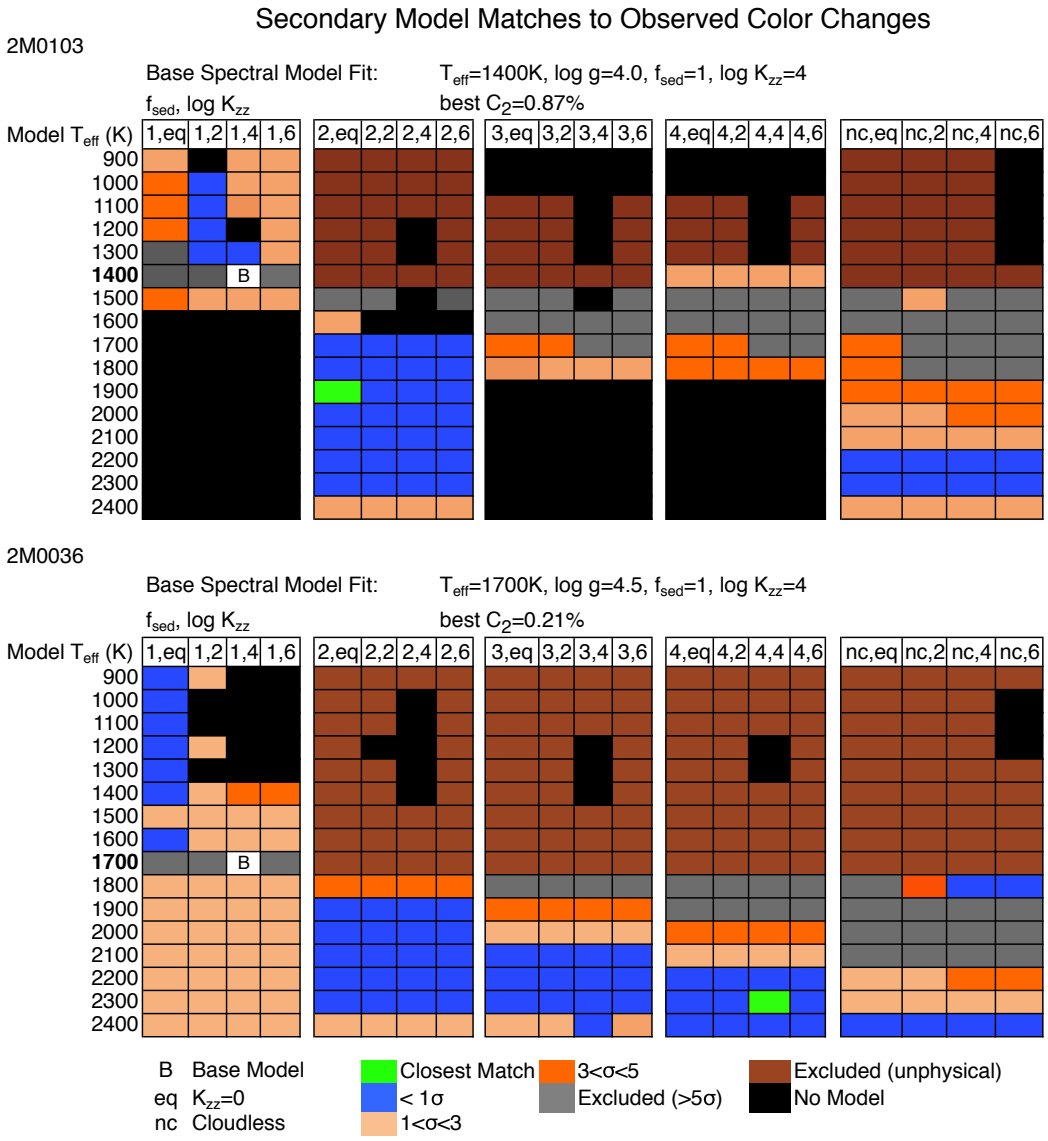

Figure 6.5 Model pair combinations reproduce the observed Ch1–Ch2 color changes for 2M0103 and 2M0036. Color key is identical to Figure 6.4. The very small amplitudes of 2M0036 produce many likely matches over a wide range of T_{eff}, and account for its extremely small value of C_2. Similarly, the $A_{Ch1}/\ A_{Ch2}$ ratio of 2M0103 (1.23) place the observed amplitudes of that dwarf within a model amplitude space where there are many likely model matches to observations.

Table 6.3. Best-Matched Model Pair Parameters for Ch1-Ch2 Color Changes

	2M2208	SDSS0107	2M0036	2M0103
T_{eff} (K)	1,400 + 1,100	$1,500 + 1,100$	$1,700 + 2,300$	$1,400 + 1,900$
$f_{\rm sed}$	$1 + 1$	$1 + 1$	$1 + 4$	$1 + 2$
K_{zz}	$10^4 + 0$	$10^4 + 0$	$10^4 + 10^4$	$10^4 + 0$
C_2	1.2%	1.8%	0.21%	0.87%
Closest distance (σ)	0.12	0.23	0.06	0.08

Ch1 and Ch2 amplitude point in A_{Ch1} and A_{Ch2} space. The model with the closest approach to the observed amplitudes point was chosen as the best match, but other model pairs that produce amplitudes within 1σ were also noted as being likely matches. Lines that had their closest approach to the observed amplitude point greater than 5σ were designated model pairs that could not produce the observed amplitudes. The results for all models, including the parameter spaces that were not covered by our model grid, are summarized in Figures 6.4 and 6.5, and the single best-matching secondary models for each dwarf are listed in Table 6.3.

In addition to considering how well the model amplitudes created from each individual secondary model in our grid compares to the observed periodic variability amplitudes of our dwarfs, we must consider if any models with parameters between our parameter grid spacing could also match the observed Spitzer amplitudes. For an example of this, consider the upper left panel of Figure 6.3. For 2M2208, a line above the blue dot (observed color changes) represents a cloud-free model of T_{eff}=1,900 K with $K_{zz} = 0$ is plotted. Below the blue dot is a line representing the cloud-free model of T_{eff}=1,900 K and log $K_{zz} = 2$. It's possible that there exists a cloudless model with T_{eff}=1,900 K, with the same gravity, but a K_{zz} between 0 and log K_{zz}=2 that would produce fluxes that would intersect the blue dot and be best-matched for our observations. We will consider any models in our parameter space that have the same T_{eff} and $f_{\rm sed}$ that straddle the observed amplitudes of the dwarf (blue dot) in K_{zz} in this way as likely matches.

With the best-fit secondary model parameters and C_2 for each dwarf determined, we can calculate how the combination of these two spectra would effect observed near infrared spectra such as ones obtained with SpeX. We do not expect observed SpeX spectra (which represents our base model) to exhibit large changes over the course of a dwarf's rotation with the assumptions we've made with our linear combination model. Figure 6.6 shows that to be the case for each of our dwarfs when combining the two best-matched model Spex-regime spectra using Equation 6.3.

6.3.4 Discussion of Two-Component Cloud Models

We present several results from our Spitzer color change model investigations by first summarizing the results for each dwarf

2M2208

The secondary models that matched within 1σ of the observed amplitudes are constrained in T_{eff} to $^{+500K}_{-400K}$ from the base model. The single best-matched secondary model has its closest approach to the dwarf's observed values at 0.12σ, with the same $f_{\rm sed} = 1$ as the base model, a T_{eff}=1,110K (–300K from the base model), and a very small C_2 value of 1.2%. All likely models have C_2 values similar to the best-matched models. Excluded models include $T_{eff} > 1600$K for $f_{\rm sed} = 2$ and the higher temperature regime for all cloudless models.

SDSS0107

SDSS0107 has only five models that are within 1σ of the observed amplitudes, which are constrained in T_{eff} to $\pm$200 K. Four out of five of these models are of the same $f_{\rm sed}$=1 as the base model, even when additionally examining the models we designated as unphysical. The single best-matched model has a T_{eff}=1,500K, $f_{\rm sed}$=1, K_{zz}=0, and a small C_2 value of 1.8%. All best-matched secondary models had similarly small values of C_2. One reason for the fewer likely secondary model matches is that SDSS0107's Ch1/Ch2 amplitudes (1.05) place the dwarf's amplitude

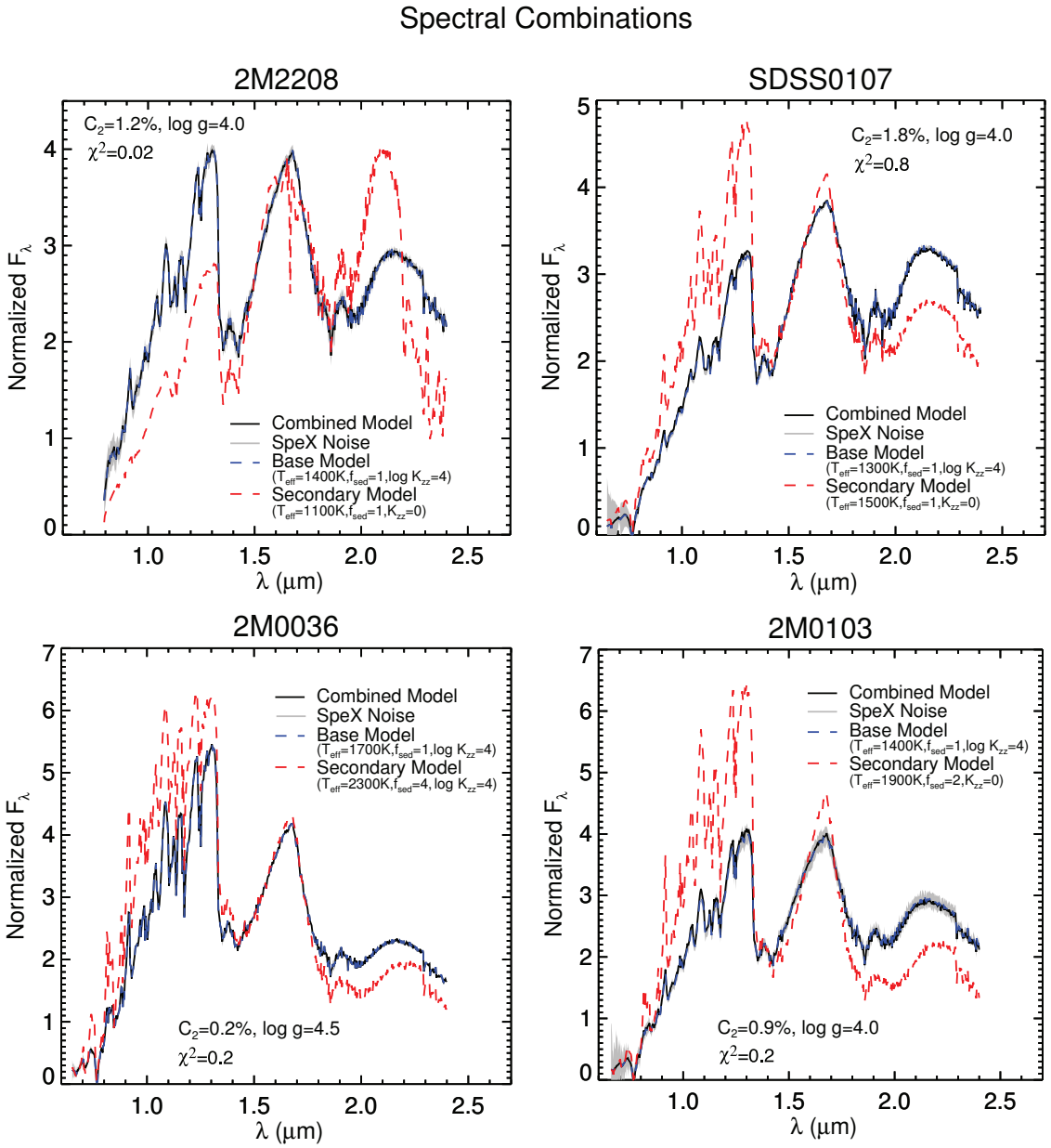

Figure 6.6 A linear combination of the best-fit SpeX-regime base and secondary model with the best-fit C_2 value are extremely close to the base model for each dwarf. Very little observed change in Spex-regime spectra is expected to be observed using the best-fit models that reproduce the variability seen in Ch1 and Ch2. Combined models were calculated according to Equation 6.3. The uncertainties from the observed SpeX spectra at each wavelength are shown, and used in a reduced χ^2 calculation between the combined and base models.

values in our model amplitude space near the edge of most of the models (as seen qualitatively in Figure 6.2). Other dwarfs have observed amplitude ratios higher than this, which put them in the range of more secondary models. If the dwarf's amplitudes were lower, it would also put more models in range of this dwarf.

2M0103

2M0103 has a range of best-matching secondary models that span range of T_{eff} that encompass much of the T_{eff} range of our model grid ($^{+900K}_{-400K}$ from the base model). The single best matching model was a model with T_{eff}=1900K, $f_{\rm sed}$=2, K_{zz}=0 and a C_2=0.87%, which was a similar C_2 to all likely secondary model matches. All but the highest T_{eff} values for K_{zz}=0 models can be excluded as being likely secondary model matches.

2M0036

Like 2M0103, 2M0036 has a wide range of best-matching $< 1\sigma$ secondary models that span the T_{eff} range of our model grid ($^{+700K}_{-800K}$ from the base model). The very small observed amplitudes (0.33 and 0.44%) for this dwarf place it even closer to the origin in A_{Ch1} and A_{Ch2} space, enabling many more models to fall within the $< 1\sigma$ range. However, with a more complete model grid in the log g=4.5 model space for this dwarf, we can see that secondary model matches generally become increasingly constrained to higher temperatures as $f_{\rm sed}$ increases.

In addition to the dwarf-specific results above, we also present the following general results:

1. When considering possible models that are between our K_{zz} model grid spacing that could reproduce our observed color changes, for SDSS0107, we find that 17 out of 18 of these possible models fall within the same ΔT_{eff} as our discretely computed models, with the outlier model at $T_{eff} = 900$K, $f_{sed} = 1$. For 2M2208, all of these possible model matches fall within the temperature range of our matches from the computed model grid, with $\Delta T = ^{+500K}_{-400K}$ from

the base model. We do not have these possibly interpolated models to confirm their fluxes, so we will include them in the best-fit range of $< 1\sigma$, but will still designate our best single matched secondary model from our discretely computed grid. For 2M0036 and 2M0103, we find that these possible interpolated models also span the ranges of T_{eff} as described above.

2. For SDSS0107 and 2M2208, the T_{eff} differences for our best-matched model pairs, as well as the secondary models that produce color changes within 1σ of the observations are generally consistent with the model pair temperature differences for cooler, periodic photometrically variable L/T dwarfs found in Apai et al. (2013, ΔT_{eff}=300 K) and Buenzli et al. (2015a,b, ΔT_{eff}=100–300 K).

3. Two key factors for a dwarf having more constraints on possible best-matching secondary models are the observed variability amplitudes and the Ch1/Ch2 amplitude ratio. Amplitude ratios that put the dwarf on the edges or in a less populated area of a model amplitude grid such as Figure 6.2 will result in many models being excluded from being best-matches, and higher amplitudes will also distance the dwarf's value from the origin in model amplitude space where all C_2 lines converge.

4. Values of C_2 that represent the closest secondary model matches to the observed color changes for all dwarfs occur at very small values, ranging from 0.21% for 2M0036 to 1.8% for SDSS0107. This indicates that a very small fraction of the secondary spectra is contributing to the observed Spitzer variations for each dwarf, and that the observed photometric periodic variability of these two L dwarfs, if due to two different cloudy surfaces with differing T_{eff}, cloud opacities and vertical mixing, is dominated by a single surface. The domination of one model spectra over the contributions of a secondary model was also found in model fitting variable L/T transition dwarfs (Buenzli et al., 2015a,b). From Figure 6.6 and the resulting low χ^2 statistic between the base and the best-fit secondary models in combination with the noise from SpeX

observations, we can see that the assumptions from our linear combination of two atmosphere models from Equation 6.3 hold; we would expect to see very little change in the NIR spectra for our dwarfs when combining the primary and secondary models that reproduce the amplitudes as seen in Spitzer, at these very low values of C_2.

5. No universal differences in T_{eff}, $f_{\rm sed}$, or K_{zz} parameters in model pairs can reproduce the observed color changes across both of our L dwarfs. Flux differences arise from changes in many combination of these parameters between the base models and possible secondary models.

6.4 Timescales of Light Curve Evolution (LCE)

In this section, we will discuss aspects of possible physical explanations for the observed timescales of light curve evolution. First we, will explore a basic model involving purely radiative dissipation in a dynamics-free atmosphere that can provide insights into future realistic brown dwarf atmosphere models. We will then separately investigate general properties of atmospheric dynamics in brown dwarfs that could result in the observed changes of our light curves.

6.4.1 Radiative Flux Variations and Time Scales

Any physically realistic model of cloudy brown dwarf atmospheres must consider the complex interaction of dynamics with the radiative properties throughout the dwarf. One source of atmospheric disturbances are changes in heating rates at various depths, which can be caused by any number of processes that include the interaction of dynamics and radiation, such as wave breaking and cloud effects. These thermal perturbations can propagate radiatively and dynamically through the atmosphere, including being altered by dynamic processes that created the perturbation, or ones that directly result from it, such as Rossby waves propagating upward through the atmospheric column. Such perturbations can lead to observed periodic photometric variability due to brightness temperature differences and cloud changes, while

also resulting in the alteration of any existing variability. The timescales that the resulting temperature differences remain in the atmosphere in these models can be compared to those in the observed periodic photometric variability and variability evolution to begin to inform us as to the responsible atmospheric processes.

Changes to dynamical wave fluxes or other details of the dynamics could easily lead to variations in the thermal perturbations and the length they can be maintained from just considering purely radiative properties of the atmosphere. (Showman and Kaspi, 2013). However, we can inform future complex models of brown dwarf atmospheres and investigations into periodic variability by exploring the relatively narrow subject of radiative time scales in a purely radiative cloudy atmosphere model.

6.4.2 Description of the Models

Robinson and Marley (2014) used a 1-D time-stepping model of the thermal structure of a dwarf's atmosphere to calculate how a theoretical change in heating rates at various atmospheric pressures would result in integrated flux changes at the surface at various bandpasses. This model was free of any dynamics or clouds. Temperature variation rates from 10 to 500 h, temperatures from 8 to 20 K that corresponded to pressure levels from 100 to 1 bar. The timescales of temperature propagation from depth ranged from 10 to 100 h, and it was noted that deep thermal perturbations lead to brightness variations at nearly all NIR wavelengths. Corresponding timescales to fully radiate away the perturbation ranged in the hundreds of hours.

In this work, we will utilize a similar, but even simpler model to investigate the radiative timescales due to purely radiative processes; our 1D model only investigates radiative dissipation vertically outward from lower to higher atmospheric depths.

6.4.3 Thermal Perturbation Procedure and Results

We selected thermal perturbation models that matched parameters of the best-fit T_{eff}, $\log g$, $f_{\rm sed}$, and K_{zz} parameters from the previous part of this work. We then

introduced a temperature perturbation into the atmospheric pressures ranging from 10^{-4} to $\sim$15 bar, which was divided into quarter scale height segments. For each trial for each dwarf, these models begin with the initial perturbed layer, calculating the perturbed temperature profile one quarter scale height at a time, moving to lower atmospheric pressures (outward) until the initial temperature perturbation has completely radiated from all layers. For each trial, a perturbed mean spectra at the top of the atmosphere was generated. Artificial photometry was then performed on the perturbed spectra for Ch1 and Ch2 using IRAC filter profiles (Hora et al., 2008), which was ratioed with flux values calculated from the unperturbed mean spectra. The amount of time needed for each temperature perturbation trial to dissipate completely from all layers was calculated. Subsequent trials for each dwarf had the perturbation beginning in a different atmospheric pressure, with new perturbation levels changing in quarter scale height increments.

The plot of these flux ratios throughout each dwarf's atmosphere is found in Figure 6.7. The peak perturbed/unperturbed flux ratio for each Spitzer channel is marked in the plots by hatched areas representing the corresponding pressure levels. These pressure levels represent the atmospheric level at which peak Spitzer Ch1 and Ch2 perturbed/unperturbed flux ratios would be generated from if a temperature perturbation was introduced there (flux from other non-peak pressure levels would also contribute if perturbations existed there, as seen in the plot). The radiative timescales for those peak perturbed/unperturbed flux ratios are noted on the plot.

6.4.4 Radiative Flux Variations and Timescales Discussion

In these radiative models, the timescales for thermal perturbations to completely dissipate from pressure levels that produce peak perturbed/unperturbed flux ratios Spitzer Ch1 and Ch2 ($\sim$0.1 bar) are $\leq$ 1.40 h for both Ch1 and Ch2 in all of our dwarfs. For all dwarfs, the radiative timescales for each perturbed level are similar for a regime of lower pressures, before entering a distinct pressure regime where the timescales begin to increase with increasing pressure (Figure 6.7, right column). For each of our dwarfs, the pressure level that produces the peak perturbed/unperturbed

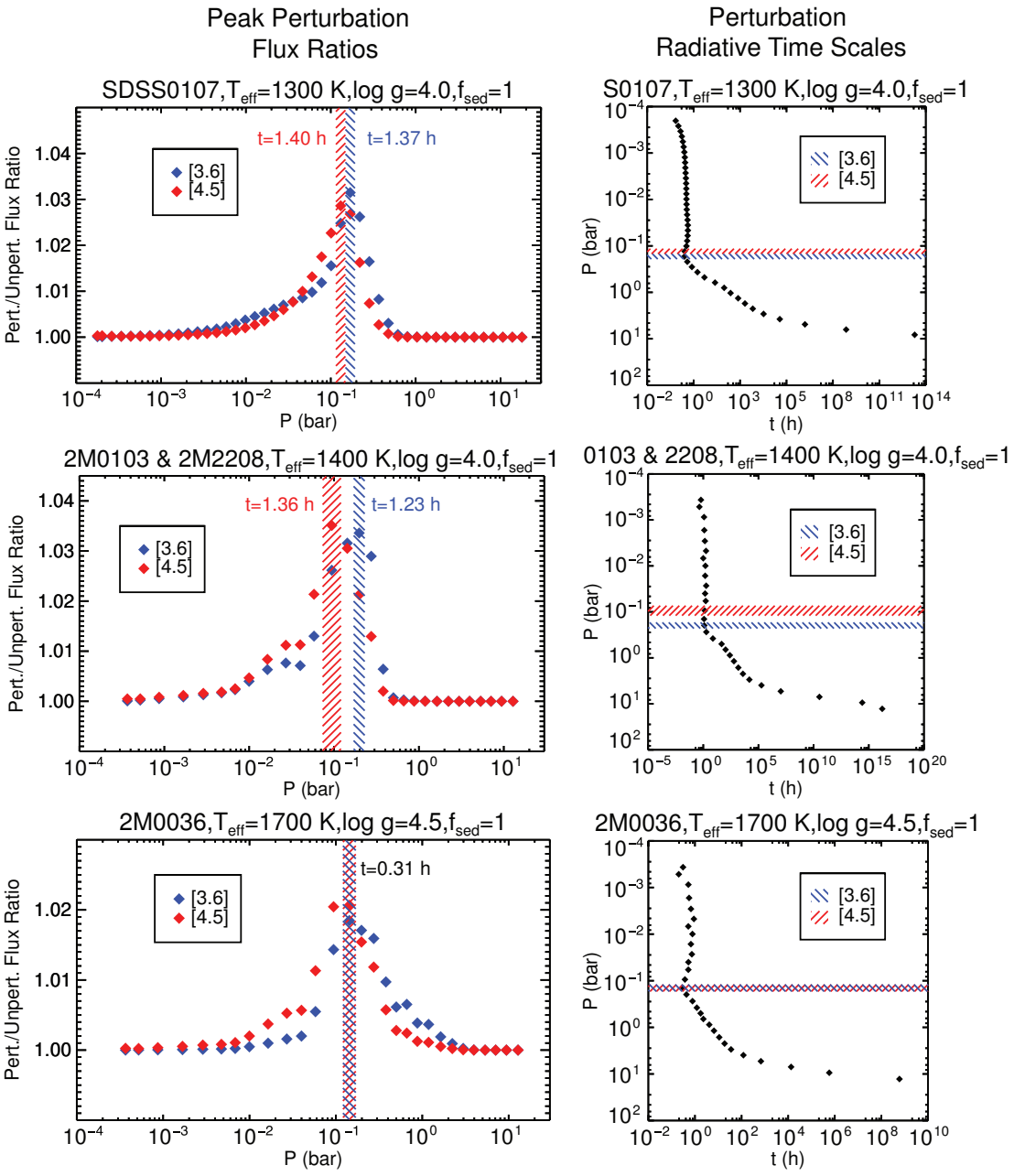

Figure 6.7 Perturbed/unperturbed flux ratios (*left column*) and radiative timescales "t" (*right column*) for each thermal perturbation in purely radiative cloudy models are shown. Hatched areas indicate the extent of pressure levels which produced peak flux ratios in Ch1 (blue) and Ch2 (red) when perturbed. Radiative timescales for dissipating perturbations initiated in the pressure level that produces peak perturbed/unperturbed flux ratios are $\leq$ 1.40 h for all dwarfs in both channels.

flux ratio as observed with Spitzer Ch1 and Ch2 is at the boundary of these two pressure regimes. Although these radiative timescales in these purely radiative models are short ($\leq$ 1 rotation period for our dwarfs), and too short to be the cause of sustained rotationally-induced variability, it's very likely that various dynamic processes will lengthen these timescales (Showman and Kaspi, 2013). The extent to which these perturbation timescales are lengthened, and the resulting atmospheric levels these perturbations are sustained in is the subject of the intersection of future dynamic and radiative modeling. If the timescales for these perturbations are not lengthened by dynamic and other processes more than an order of magnitude, such perturbations at these depth could still be responsible for the light curve evolution as seen in our Spitzer light curves.

6.4.5 Dynamical Processes and Timescales

Our light curves exhibit variations of $\sim$0.3–2% relative amplitudes with structure that is sufficiently periodic to suggest rotational modulations on timescales of $\sim$3–10 hours, and yet the light curve structure nevertheless evolves from one period to the next. To provide context for understanding this variability, it is interesting to consider the types of dynamical behavior expected on brown dwarfs. Showman and Kaspi (2013) presented an analytic theory for the dynamics of the stratified atmosphere of brown dwarfs which allowed predictions for the wind speeds and temperature perturbations associated with the circulation. In their theory, interior convection triggers waves and small-scale turbulence in the atmosphere, which interact with the mean flow to generate large-scale atmospheric structures such as vortices and/or zonal jet streams. Depending on the assumed efficiency of the wave driving, their theory predicts wind speeds of tens to hundreds of m/sec and horizontal temperature perturbations (on isobars) of several to $\sim$ 50 K. A large-scale overturning (e.g., meridional) circulation will accompany this stratified turbulence, with the regions of ascent and descent organized at large scale. Because regions of ascent would lead to cloudiness, whereas regions of descent would tend to be less cloudy, their theory implies the presence of cloud patchiness. Since radiation escapes

to space from significantly greater pressure in the less-cloudy regions, there can be large differences in brightness temperature between cloudy and cloud-free regions, allowing the existence of significant rotational modulation in light curves.

Dynamical studies to date provide guidance on the key length scales of the atmospheric circulation. The Rossby deformation radius, L_D, represents a natural scale for the interaction of buoyancy and rotation, and as a result, vortices and turbulent eddies often have a characteristic size similar to the deformation radius. On brown dwarfs, L_D is typically a few thousand km (Zhang and Showman, 2014). Another key flow length scale is the Rhines scale, which is a typical size scale at which zonal banding becomes prominent (for reviews, see Vasavada and Showman 2005, Showman et al. 2010). The Rhines scale is $\pi(U/\beta)^{1/2}$, where $\beta = 2\Omega \sin\phi/a$ is the gradient of Coriolis parameter with northward distance, Ω is rotation rate, ϕ is latitude, and a is the brown dwarf radius. Given a rotation period of 5 hours, a Jupiter radius, and wind speeds ranging from 30 to 300 m/sec, one obtains a Rhines scale of ∼5,000 to 20,000 km. This is the likely scale of any zonal jets that exist. Nevertheless, Zhang and Showman (2014) showed that, for sufficiently short radiative timescales, it is possible for the radiation to damp turbulent structures before they have time to reorganize into zonal jets. Thus, the question of whether zonal banding exists on our L dwarfs remains open.

To provide guidance in understanding the evolution of our light curves, estimating relevant dynamical timescales is useful. The advection timescale for air to advect over a brown dwarf radius, a/U, where a is the radius and U is the wind speed, is $\sim 2 \times 10^5$–2×10^6 sec for wind speeds of 30–300 m/sec. In contrast, the horizontal advection time across a deformation radius is significantly shorter — 10^4–10^5 sec for wind speeds of 30–300 m/sec. This is the timescale over which individual vortices could change significantly in shape or structure. Moreover, mass continuity then suggests that the vertical advection time over a distance comparable to the vertical scale of the circulation (likely to be of order a scale height) is also $\sim 10^4$–10^5 sec. Thus, significant changes to the cloud structure of individual eddies or vortices could occur over these timescales, causing gradual changes to observed IR light curves on

these timescales. Given a rotation period of 5 h, this implies gradual changes to the light curve shape on timescales of 0.5 to 5 rotation periods. Complete "loss of memory" in the light curve (i.e. complete scrambling of the phase and shape of the light curve from some earlier state) is likely to take place on timescales comparable to advection over a brown-dwarf radius, which is 10–100 brown dwarf rotation periods (Showman and Kaspi, 2013; Zhang and Showman, 2014). These estimates are consistent with, and help to explain, the changes in shape of our light curves and other dwarf light curves (e.g. Artigau et al. 2009) on timescales of several rotation periods. Further detailed modeling of the connection between dynamical structure and light curve evolution would be extremely beneficial.

Another issue concerns the differing behavior in Ch1 and Ch2 light curves for SDSS0107 and the seeming lagged correlation between the two curves. This behavior implies that the spatial pattern of patchiness at the time of our observations must differ significantly between the two channels. Buenzli et al. (2012) considered a number of scenarios by which this could come about, including the possibility of stacked circulation cells and multiple cloud decks that exhibit differing spatial patterns of patchiness, with differing wavebands (e.g., Ch1 and Ch2) sampling different vertical regions within this complex structure. Nevertheless, these possibilities remain qualitative and further work on the question is clearly warranted.

CHAPTER 7

CONCLUSIONS AND SUMMARY

All four of the L dwarfs in this study are clearly photometrically variable in the Spitzer [3.6] and [4.5] bandpasses, with relative amplitudes ranging from 0.3–1.8%, with measured rotation periods from 2.6–10.2 h. The light curves in the two channels for a given object are similar, but with shape and amplitude differences. Two of the four objects have double-peaked light curves. We also observe light curve evolution for two of our L dwarfs, with timescales ranging from as short as a few hours, to the observed longer term brightening trend of 2M0103 in Ch1 of $\sim 0.5\%$. Similarities in the Ch1 and Ch2 light curves for SDSS0107 with the strongest correlation occurring at a 90.5 degrees difference of the Ch1 period is observed, indicating a possible correlation of the same global cloud structures through the different pressure-layers probed by the Spitzer bandpasses.

Observed Ch1–Ch2 color changes are well explained for SDSS0107 and 2M2208 as a combination of two model cloudy surfaces (for SDSS0107, 21/22 possible matches $\Delta T_{eff} = \pm 200$K from the base model and for 2M2208, $\Delta T_{eff} = ^{+500K}_{-400K}$ from the base model). Best-matched model pairs with various differences in T_{eff}, $f_{\rm sed}$ and K_{zz} are able to reproduce the observed periodic photometric amplitudes. The large number of possible secondary model matches over a wide range of T_{eff} for 2M0036 and 2M0103 can be attributed to relatively higher observed [3.6]/[4.5] amplitude ratios and in the case of 2M0036, very low observed amplitude values. Small secondary model contribution fractions between all base and secondary models indicate that the atmospheres are dominated by one surface, with only very small contributions from a secondary spectral model needed to produce the observed amplitudes in both Spitzer channels.

Fit to SpeX spectra and Spitzer fluxes provide further evidence of the low-gravity nature of the L3γ dwarf 2M2208, with evolutionary models indicating that 2M2208

is a young ∼10 Myr planetary mass object of ∼8 $M_{\rm Jup}$.

Exploration of purely radiative cloudy models can inform us about the very basic radiative timescales that are associated with thermal perturbations within these model atmospheres. Thermal perturbations using these models indicate that these basic radiative timescales are short ($\leq$ 1.40 h) for thermal perturbations at the atmospheric levels that produce peak perturbed/unperturbed flux ratios in both Spitzer channels. Dynamic and radiative processes are tightly coupled in real brown dwarf atmospheres, and those processes are likely to alter these timescales. Future models that incorporate dynamics and radiative properties of cloudy atmospheres can ultimately investigate the final form of these perturbations as they propagate through a more realistic model atmosphere. However, these radiative timescales can be lengthened by an order of magnitude and still be a candidate as a source for some of our short-term light curve evolution.

Recent dynamical studies in brown dwarf atmospheres provide insight into the atmospheric sources of variability due to cloud patchiness and the evolution of light curves over time. Large-scale overturning circulations and stratified turbulence can lead to patchy clouds and differences in brightness temperatures between observed surfaces. Light curve evolution can be the result of horizontal and vertical advection, which have similar timescales of ∼3–28 h, which overlaps the rotational periods of all of our periodic L–dwarfs and the observed short-term light curve evolution. Qualitative possibilities have been previously put forward for previous NIR phase shifts in brown dwarfs that may help to explain the light curve correlations found in SDSS0107, including stacked circulation cells and multiple cloud decks that exhibit differing spatial patterns of patchiness.

We note that the mechanisms of any long-term changes in periodic photometric variability and overall luminosity changes of ultracool dwarfs over a period of years can be explored, now that there exists a 10+ year photometric history of some variable dwarfs. One of the most robust investigations into the evolution of periodic photometric variability that can address these issues is the Spitzer Extrasolar Storms campaign (GO:90063, PI: Apai), which, when completed, will have monitored six

known variable brown dwarfs spanning a wide range of spectral types and rotation periods with high precision Ch1 and Ch2 photometry for up to a year.

7.1 Summary

We summarize our key results as follows:

1. Photometric Ch1–Ch2 color changes are well described for two of our dwarfs as a combination of two model cloudy surfaces, with possible secondary model matches with $\Delta T_{eff} = \pm 200$ K and $^{+500K}_{-400K}$. Model pairs that differ in T_{eff}, $f_{\rm sed}$ and K_{zz} are able to reproduce the observed amplitudes. Dwarfs with higher amplitudes and lower [3.6]/[4.5] amplitude ratios are more easily described by a small number of secondary models. Small secondary model contribution fractions between base and secondary models indicate that the atmosphere is dominated by one cloud type with only small contributions from a secondary spectral model needed to produce the observed Spitzer color changes.

2. Through spectral and flux fitting and with evolutionary models, we provide additional evidence of the low gravity nature of L3γ dwarf 2M2208, and note it as a young $\sim$10 Myr planetary mass object of $\sim$8 $M_{\rm Jup}$

3. Purely radiative model temperature perturbations at atmospheric depths that produce peak perturbed/unperturbed flux ratios in [3.6] and [4.5] channels have short radiative timescales ($\leq$ 1.40 h) for our L dwarfs. Dynamic and radiative processes are likely to lengthen these dissipation timescales from these simple models, but they can be lengthened by an order of magnitude and still be in the range of some of the observed light curve evolution of our dwarfs, indicating that thermal perturbations that arise from a variety of sources could result in short-term light curve evolution in brown dwarfs. Atmospheric dynamic mechanisms that can effect cloud composition, temperature and distribution can also be likely sources of this light curve evolution.

REFERENCES

Ackerman, A. S. and M. S. Marley (2001). Precipitating Condensation Clouds in Substellar Atmospheres. *ApJ*, **556**, pp. 872–884. doi: 10.1086/321540.

Alexander, T. (1997). Is AGN Variability Correlated with Other AGN Properties? ZDCF Analysis of Small Samples of Sparse Light Curves. In Maoz, D., A. Sternberg, and E. M. Leibowitz (eds.) *Astronomical Time Series*, volume 218 of *Astrophysics and Space Science Library*, p. 163.

Allen, P. R., D. W. Koerner, M. W. McElwain, K. L. Cruz, and I. N. Reid (2007). A New Brown Dwarf Desert? A Scarcity of Wide Ultracool Binaries. *AJ*, **133**, pp. 971–978. doi: 10.1086/510346.

Allers, K. N. and M. C. Liu (2013). A Near-infrared Spectroscopic Study of Young Field Ultracool Dwarfs. *ApJ*, **772**, 79. doi: 10.1088/0004-637X/772/2/79.

Andersen, M., M. R. Meyer, J. Greissl, and A. Aversa (2008). Evidence for a Turnover in the Initial Mass Function of Low-Mass Stars and Substellar Objects: Analysis from an Ensemble of Young Clusters. *ApJ*, **683**, pp. L183–L186. doi: 10.1086/591473.

Apai, D., J. Radigan, E. Buenzli, A. Burrows, I. N. Reid, and R. Jayawardhana (2013). HST Spectral Mapping of L/T Transition Brown Dwarfs Reveals Cloud Thickness Variations. *ApJ*, **768**, 121. doi: 10.1088/0004-637X/768/2/121.

Artigau, É., S. Bouchard, R. Doyon, and D. Lafrenière (2009). Photometric Variability of the T2.5 Brown Dwarf SIMP J013656.5+093347: Evidence for Evolving Weather Patterns. *ApJ*, **701**, pp. 1534–1539. doi: 10.1088/0004-637X/701/2/1534.

Atreya, S. K., M. H. Wong, T. C. Owen, P. R. Mahaffy, H. B. Niemann, I. de Pater, P. Drossart, and T. Encrenaz (1999). A comparison of the atmospheres of Jupiter and Saturn: deep atmospheric composition, cloud structure, vertical mixing, and origin. *Planet. Space Sci.*, **47**, pp. 1243–1262. doi: 10.1016/S0032-0633(99)00047-1.

Bailer-Jones, C. A. L. and R. Mundt (2001). Variability in ultra cool dwarfs: Evidence for the evolution of surface features. *A&A*, **367**, pp. 218–235. doi: 10.1051/0004-6361:20000416.

Berger, E. (2002). Flaring up All Over-Radio Activity in Rapidly Rotating Late M and L Dwarfs. *ApJ*, **572**, pp. 503–513. doi: 10.1086/340301.

Bjoraker, G. L., H. P. Larson, and V. G. Kunde (1986). The abundance and distribution of water vapor in Jupiter's atmosphere. *ApJ*, **311**, pp. 1058–1072. doi: 10.1086/164842.

Blake, C. H., D. Charbonneau, and R. J. White (2010). The NIRSPEC Ultracool Dwarf Radial Velocity Survey. *ApJ*, **723**, pp. 684–706. doi: 10.1088/0004-637X/723/1/684.

Bouy, H., W. Brandner, E. L. Martín, X. Delfosse, F. Allard, and G. Basri (2003). Multiplicity of Nearby Free-Floating Ultracool Dwarfs: A Hubble Space Telescope WFPC2 Search for Companions. *AJ*, **126**, pp. 1526–1554. doi: 10.1086/377343.

Buenzli, E., D. Apai, C. V. Morley, D. Flateau, A. P. Showman, A. Burrows, M. S. Marley, N. K. Lewis, and I. N. Reid (2012). Vertical Atmospheric Structure in a Variable Brown Dwarf: Pressure-dependent Phase Shifts in Simultaneous Hubble Space Telescope-Spitzer Light Curves. *ApJ*, **760**, L31. doi: 10.1088/2041-8205/760/2/L31.

Buenzli, E., D. Apai, J. Radigan, C. Morley, A. Burrows, D. Flateau, A. Showman, M. Marley, I. N. Reid, N. Lewis, and R. Jayawardhana (2013). Probing the Heterogeneous Cloud Structure of Variable Brown Dwarfs with HST. In *Protostars and Planets VI Posters*, p. 23.

Buenzli, E., D. Apai, J. Radigan, I. N. Reid, and D. Flateau (2014). Brown Dwarf Photospheres are Patchy: A Hubble Space Telescope Near-infrared Spectroscopic Survey Finds Frequent Low-level Variability. *ApJ*, **782**, 77. doi: 10.1088/0004-637X/782/2/77.

Buenzli, E., M. S. Marley, D. Apai, D. Saumon, B. A. Biller, I. J. M. Crossfield, and J. Radigan (2015a). Cloud Structure of the Nearest Brown Dwarfs II: High-amplitude variability for Luhman 16 A and B in and out of the 0.99 micron FeH feature. *ArXiv e-prints*.

Buenzli, E., D. Saumon, M. S. Marley, D. Apai, J. Radigan, L. R. Bedin, I. N. Reid, and C. V. Morley (2015b). Cloud Structure of the Nearest Brown Dwarfs: Spectroscopic Variability of Luhman 16AB from the Hubble Space Telescope. *ApJ*, **798**, 127. doi: 10.1088/0004-637X/798/2/127.

Burgasser, A. J., K. L. Cruz, M. Cushing, C. R. Gelino, D. L. Looper, J. K. Faherty, J. D. Kirkpatrick, and I. N. Reid (2010). SpeX Spectroscopy of Unresolved Very Low Mass Binaries. I. Identification of 17 Candidate Binaries Straddling the L Dwarf/T Dwarf Transition. *ApJ*, **710**, pp. 1142–1169. doi: 10.1088/0004-637X/710/2/1142.

Burgasser, A. J., T. R. Geballe, S. K. Leggett, J. D. Kirkpatrick, and D. A. Golimowski (2006). A Unified Near-Infrared Spectral Classification Scheme for T Dwarfs. *ApJ*, **637**, pp. 1067–1093. doi: 10.1086/498563.

Burgasser, A. J., M. C. Liu, M. J. Ireland, K. L. Cruz, and T. J. Dupuy (2008). Subtle Signatures of Multiplicity in Late-type Dwarf Spectra: The Unresolved M8.5 + T5 Binary 2MASS J03202839-0446358. *ApJ*, **681**, pp. 579–593. doi: 10.1086/588379.

Burgasser, A. J., M. S. Marley, A. S. Ackerman, D. Saumon, K. Lodders, C. C. Dahn, H. C. Harris, and J. D. Kirkpatrick (2002). Evidence of Cloud Disruption in the L/T Dwarf Transition. *ApJ*, **571**, pp. L151–L154. doi: 10.1086/341343.

Burningham, B., C. V. Cardoso, L. Smith, S. K. Leggett, R. L. Smart, A. W. Mann, S. Dhital, P. W. Lucas, C. G. Tinney, D. J. Pinfield, Z. Zhang, C. Morley, D. Saumon, K. Aller, S. P. Littlefair, D. Homeier, N. Lodieu, N. Deacon, M. S. Marley, L. van Spaandonk, D. Baker, F. Allard, A. H. Andrei, J. Canty, J. Clarke, A. C. Day-Jones, T. Dupuy, J. J. Fortney, J. Gomes, M. Ishii, H. R. A. Jones, M. Liu, A. Magazzú, F. Marocco, D. N. Murray, B. Rojas-Ayala, and M. Tamura (2013). 76 T dwarfs from the UKIDSS LAS: benchmarks, kinematics and an updated space density. *MNRAS*, **433**, pp. 457–497. doi: 10.1093/mnras/stt740.

Carlson, B. E., A. A. Lacis, and W. B. Rossow (1994). Belt-zone variations in the Jovian cloud structure. *J. Geophys. Res.*, **99**, p. 14623. doi: 10.1029/94JE01222.

Chabrier, G. and M. Küker (2006). Large-scale αˆ2-dynamo in low-mass stars and brown dwarfs. *A&A*, **446**, pp. 1027–1037. doi: 10.1051/0004-6361:20042475.

Charbonneau, D., L. E. Allen, S. T. Megeath, G. Torres, R. Alonso, T. M. Brown, R. L. Gilliland, D. W. Latham, G. Mandushev, F. T. O'Donovan, and A. Sozzetti (2005). Detection of Thermal Emission from an Extrasolar Planet. *ApJ*, **626**, pp. 523–529. doi: 10.1086/429991.

Chiu, K., X. Fan, S. K. Leggett, D. A. Golimowski, W. Zheng, T. R. Geballe, D. P. Schneider, and J. Brinkmann (2006). Seventy-One New L and T Dwarfs from the Sloan Digital Sky Survey. *AJ*, **131**, pp. 2722–2736. doi: 10.1086/501431.

Clarke, F. J., B. R. Oppenheimer, and C. G. Tinney (2002a). A mini-survey for variability in early L dwarfs. *MNRAS*, **335**, pp. 1158–1162. doi: 10.1046/j.1365-8711.2002.05691.x.

Clarke, F. J., C. G. Tinney, and K. R. Covey (2002b). Periodic photometric variability of the brown dwarf Kelu-1. *MNRAS*, **332**, pp. 361–366. doi: 10.1046/j.1365-8711.2002.05308.x.

Clarke, F. J., C. G. Tinney, and S. T. Hodgkin (2003). Time-resolved spectroscopy of the variable brown dwarf Kelu-1*. *MNRAS*, **341**, pp. 239–246. doi: 10.1046/j.1365-8711.2003.06405.x.

Cruz, K. L., A. J. Burgasser, I. N. Reid, and J. Liebert (2004). 2MASS J05185995-2828372: Discovery of an Unresolved L/T Binary. *ApJ*, **604**, pp. L61–L64. doi: 10.1086/383415.

Cruz, K. L., J. D. Kirkpatrick, and A. J. Burgasser (2009). Young L Dwarfs Identified in the Field: A Preliminary Low-Gravity, Optical Spectral Sequence from L0 to L5. *AJ*, **137**, pp. 3345–3357. doi: 10.1088/0004-6256/137/2/3345.

Cushing, M. C., J. D. Kirkpatrick, C. R. Gelino, R. L. Griffith, M. F. Skrutskie, A. Mainzer, K. A. Marsh, C. A. Beichman, A. J. Burgasser, L. A. Prato, R. A. Simcoe, M. S. Marley, D. Saumon, R. S. Freedman, P. R. Eisenhardt, and E. L. Wright (2011). The Discovery of Y Dwarfs using Data from the Wide-field Infrared Survey Explorer (WISE). *ApJ*, **743**, 50. doi: 10.1088/0004-637X/743/1/50.

Cushing, M. C., M. S. Marley, D. Saumon, B. C. Kelly, W. D. Vacca, J. T. Rayner, R. S. Freedman, K. Lodders, and T. L. Roellig (2008). Atmospheric Parameters of Field L and T Dwarfs. *ApJ*, **678**, pp. 1372–1395. doi: 10.1086/526489.

Cushing, M. C., T. L. Roellig, M. S. Marley, D. Saumon, S. K. Leggett, J. D. Kirkpatrick, J. C. Wilson, G. C. Sloan, A. K. Mainzer, J. E. Van Cleve, and J. R. Houck (2006). A Spitzer Infrared Spectrograph Spectral Sequence of M, L, and T Dwarfs. *ApJ*, **648**, pp. 614–628. doi: 10.1086/505637.

Dahn, C. C., H. C. Harris, F. J. Vrba, H. H. Guetter, B. Canzian, A. A. Henden, S. E. Levine, C. B. Luginbuhl, A. K. B. Monet, D. G. Monet, J. R. Pier, R. C. Stone, R. L. Walker, A. J. Burgasser, J. E. Gizis, J. D. Kirkpatrick, J. Liebert, and I. N. Reid (2002). Astrometry and Photometry for Cool Dwarfs and Brown Dwarfs. *AJ*, **124**, pp. 1170–1189. doi: 10.1086/341646.

Dantona, F. and I. Mazzitelli (1985). Evolution of very low mass stars and brown dwarfs. I - The minimum main-sequence mass and luminosity. *ApJ*, **296**, pp. 502–513. doi: 10.1086/163470.

Davies, S. R. (1990). An improved test for periodicity. *MNRAS*, **244**, pp. 93–95.

Dupuy, T. J. and M. C. Liu (2012). The Hawaii Infrared Parallax Program. I. Ultracool Binaries and the L/T Transition. *ApJS*, **201**, 19. doi: 10.1088/0067-0049/201/2/19.

Enoch, M. L., M. E. Brown, and A. J. Burgasser (2003). Photometric Variability at the L/T Dwarf Boundary. *AJ*, **126**, pp. 1006–1016. doi: 10.1086/376598.

Epchtein, N., E. Deul, S. Derriere, J. Borsenberger, D. Egret, G. Simon, C. Alard, L. G. Balázs, B. de Batz, M.-R. Cioni, E. Copet, M. Dennefeld, T. Forveille, P. Fouqué, F. Garzón, H. J. Habing, A. Holl, J. Hron, S. Kimeswenger, F. Lacombe, T. Le Bertre, C. Loup, G. A. Mamon, A. Omont, G. Paturel, P. Persi, A. C. Robin, D. Rouan, D. Tiphène, I. Vauglin, and S. J. Wagner (1999). A preliminary database of DENIS point sources. *A&A*, **349**, pp. 236–242.

Faherty, J. K., A. J. Burgasser, F. M. Walter, N. Van der Bliek, M. M. Shara, K. L. Cruz, A. A. West, F. J. Vrba, and G. Anglada-Escudé (2012). The Brown Dwarf Kinematics Project (BDKP). III. Parallaxes for 70 Ultracool Dwarfs. *ApJ*, **752**, 56. doi: 10.1088/0004-637X/752/1/56.

Fegley, B., Jr. and K. Lodders (1994). Chemical models of the deep atmospheres of Jupiter and Saturn. *Icarus*, **110**, pp. 117–154. doi: 10.1006/icar.1994.1111.

Freedman, R. S., J. Lustig-Yaeger, J. J. Fortney, R. E. Lupu, M. S. Marley, and K. Lodders (2014). Gaseous Mean Opacities for Giant Planet and Ultracool Dwarf Atmospheres over a Range of Metallicities and Temperatures. *ApJS*, **214**, 25. doi: 10.1088/0067-0049/214/2/25.

Freytag, B., F. Allard, H.-G. Ludwig, D. Homeier, and M. Steffen (2010). The role of convection, overshoot, and gravity waves for the transport of dust in M dwarf and brown dwarf atmospheres. *A&A*, **513**, A19. doi: 10.1051/0004-6361/200913354.

Gagné, J., D. Lafrenière, R. Doyon, L. Malo, and É. Artigau (2014). BANYAN. II. Very Low Mass and Substellar Candidate Members to Nearby, Young Kinematic Groups with Previously Known Signs of Youth. *ApJ*, **783**, 121. doi: 10.1088/0004-637X/783/2/121.

Geballe, T. R., G. R. Knapp, S. K. Leggett, X. Fan, D. A. Golimowski, S. Anderson, J. Brinkmann, I. Csabai, J. E. Gunn, S. L. Hawley, G. Hennessy, T. J. Henry, G. J. Hill, R. B. Hindsley, Ž. Ivezić, R. H. Lupton, A. McDaniel, J. A. Munn, V. K. Narayanan, E. Peng, J. R. Pier, C. M. Rockosi, D. P. Schneider, J. A. Smith, M. A. Strauss, Z. I. Tsvetanov, A. Uomoto, D. G. York, and W. Zheng (2002). Toward Spectral Classification of L and T Dwarfs: Infrared and Optical Spectroscopy and Analysis. *ApJ*, **564**, pp. 466–481. doi: 10.1086/324078.

Girardin, F., É. Artigau, and R. Doyon (2013). In Search of Dust Clouds: Photometric Monitoring of a Sample of Late L and T Dwarfs. *ApJ*, **767**, 61. doi: 10.1088/0004-637X/767/1/61.

Golimowski, D. A., S. K. Leggett, M. S. Marley, X. Fan, T. R. Geballe, G. R. Knapp, F. J. Vrba, A. A. Henden, C. B. Luginbuhl, H. H. Guetter, J. A. Munn, B. Canzian, W. Zheng, Z. I. Tsvetanov, K. Chiu, K. Glazebrook, E. A. Hoversten,

D. P. Schneider, and J. Brinkmann (2004). L' and M' Photometry of Ultracool Dwarfs. *AJ*, **127**, pp. 3516–3536. doi: 10.1086/420709.

Griffith, C. A. and R. V. Yelle (1999). Disequilibrium Chemistry in a Brown Dwarf's Atmosphere: Carbon Monoxide in Gliese 229B. *ApJ*, **519**, pp. L85–L88. doi: 10.1086/312103.

Hallinan, G., A. Antonova, J. G. Doyle, S. Bourke, C. Lane, and A. Golden (2008). Confirmation of the Electron Cyclotron Maser Instability as the Dominant Source of Radio Emission from Very Low Mass Stars and Brown Dwarfs. *ApJ*, **684**, pp. 644–653. doi: 10.1086/590360.

Hawley, S. L., K. R. Covey, G. R. Knapp, D. A. Golimowski, X. Fan, S. F. Anderson, J. E. Gunn, H. C. Harris, Ž. Ivezić, G. M. Long, R. H. Lupton, P. M. McGehee, V. Narayanan, E. Peng, D. Schlegel, D. P. Schneider, E. Y. Spahn, M. A. Strauss, P. Szkody, Z. Tsvetanov, L. M. Walkowicz, J. Brinkmann, M. Harvanek, G. S. Hennessy, S. J. Kleinman, J. Krzesinski, D. Long, E. H. Neilsen, P. R. Newman, A. Nitta, S. A. Snedden, and D. G. York (2002). Characterization of M, L, and T Dwarfs in the Sloan Digital Sky Survey. *AJ*, **123**, pp. 3409–3427. doi: 10.1086/340697.

Hayashi, C. and T. Nakano (1963). Evolution of Stars of Small Masses in the Pre-Main-Sequence Stages. *Progress of Theoretical Physics*, **30**, pp. 460–474. doi: 10.1143/PTP.30.460.

Heinze, A. N., S. Metchev, D. Apai, D. Flateau, R. Kurtev, M. Marley, J. Radigan, A. J. Burgasser, É. Artigau, and P. Plavchan (2013). Weather on Other Worlds. I. Detection of Periodic Variability in the L3 Dwarf DENIS-P J1058.7-1548 with Precise Multi-wavelength Photometry. *ApJ*, **767**, 173. doi: 10.1088/0004-637X/767/2/173.

Heinze, A. N., S. Metchev, and K. Kellogg (2015). Weather on Other Worlds. III. A Survey for T Dwarfs with High-amplitude Optical Variability. *ApJ*, **801**, 104. doi: 10.1088/0004-637X/801/2/104.

Hora, J. L., S. Carey, J. Surace, M. Marengo, P. Lowrance, W. J. Glaccum, M. Lacy, W. T. Reach, W. F. Hoffmann, P. Barmby, S. P. Willner, G. G. Fazio, S. T. Megeath, L. E. Allen, B. Bhattacharya, and M. Quijada (2008). Photometry using the Infrared Array Camera on the Spitzer Space Telescope. *PASP*, **120**, pp. 1233–1243. doi: 10.1086/593217.

Jameson, R. F., N. Lodieu, S. L. Casewell, N. P. Bannister, and P. D. Dobbie (2008). The ages of L dwarfs. *MNRAS*, **385**, pp. 1771–1778. doi: 10.1111/j.1365-2966.2008.12973.x.

Khandrika, H., A. J. Burgasser, C. Melis, C. Luk, E. Bowsher, and B. Swift (2013). A Search for Photometric Variability in L- and T-type Brown Dwarf Atmospheres. *AJ*, **145**, 71. doi: 10.1088/0004-6256/145/3/71.

Kirkpatrick, J. D., K. L. Cruz, T. S. Barman, A. J. Burgasser, D. L. Looper, C. G. Tinney, C. R. Gelino, P. J. Lowrance, J. Liebert, J. M. Carpenter, L. A. Hillenbrand, and J. R. Stauffer (2008). A Sample of Very Young Field L Dwarfs and Implications for the Brown Dwarf "Lithium Test" at Early Ages. *ApJ*, **689**, pp. 1295–1326. doi: 10.1086/592768.

Kirkpatrick, J. D., M. C. Cushing, C. R. Gelino, R. L. Griffith, M. F. Skrutskie, K. A. Marsh, E. L. Wright, A. Mainzer, P. R. Eisenhardt, I. S. McLean, M. A. Thompson, J. M. Bauer, D. J. Benford, C. R. Bridge, S. E. Lake, S. M. Petty, S. A. Stanford, C.-W. Tsai, V. Bailey, C. A. Beichman, J. S. Bloom, J. J. Bochanski, A. J. Burgasser, P. L. Capak, K. L. Cruz, P. M. Hinz, J. S. Kartaltepe, R. P. Knox, S. Manohar, D. Masters, M. Morales-Calderón, L. A. Prato, T. J. Rodigas, M. Salvato, S. D. Schurr, N. Z. Scoville, R. A. Simcoe, K. R. Stapelfeldt, D. Stern, N. D. Stock, and W. D. Vacca (2011). The First Hundred Brown Dwarfs Discovered by the Wide-field Infrared Survey Explorer (WISE). *ApJS*, **197**, 19. doi: 10.1088/0067-0049/197/2/19.

Kirkpatrick, J. D., C. C. Dahn, D. G. Monet, I. N. Reid, J. E. Gizis, J. Liebert, and A. J. Burgasser (2001). Brown Dwarf Companions to G-Type Stars. I. Gliese 417B and Gliese 584C. *AJ*, **121**, pp. 3235–3253. doi: 10.1086/321085.

Kirkpatrick, J. D., T. J. Henry, and D. W. McCarthy, Jr. (1991). A standard stellar spectral sequence in the red/near-infrared - Classes K5 to M9. *ApJS*, **77**, pp. 417–440. doi: 10.1086/191611.

Kirkpatrick, J. D., I. N. Reid, J. Liebert, R. M. Cutri, B. Nelson, C. A. Beichman, C. C. Dahn, D. G. Monet, J. E. Gizis, and M. F. Skrutskie (1999). Dwarfs Cooler than "M": The Definition of Spectral Type "L" Using Discoveries from the 2 Micron All-Sky Survey (2MASS). *ApJ*, **519**, pp. 802–833. doi: 10.1086/307414.

Kirkpatrick, J. D., I. N. Reid, J. Liebert, J. E. Gizis, A. J. Burgasser, D. G. Monet, C. C. Dahn, B. Nelson, and R. J. Williams (2000). 67 Additional L Dwarfs Discovered by the Two Micron All Sky Survey. *AJ*, **120**, pp. 447–472. doi: 10.1086/301427.

Knapp, G. R., S. K. Leggett, X. Fan, M. S. Marley, T. R. Geballe, D. A. Golimowski, D. Finkbeiner, J. E. Gunn, J. Hennawi, Z. Ivezić, R. H. Lupton, D. J. Schlegel, M. A. Strauss, Z. I. Tsvetanov, K. Chiu, E. A. Hoversten, K. Glazebrook, W. Zheng, M. Hendrickson, C. C. Williams, A. Uomoto, F. J. Vrba, A. A. Henden, C. B. Luginbuhl, H. H. Guetter, J. A. Munn, B. Canzian, D. P. Schneider,

and J. Brinkmann (2004). Near-Infrared Photometry and Spectroscopy of L and T Dwarfs: The Effects of Temperature, Clouds, and Gravity. *AJ*, **127**, pp. 3553–3578. doi: 10.1086/420707.

Knutson, H. A., D. Charbonneau, L. E. Allen, A. Burrows, and S. T. Megeath (2008). The 3.6-8.0 μm Broadband Emission Spectrum of HD 209458b: Evidence for an Atmospheric Temperature Inversion. *ApJ*, **673**, pp. 526–531. doi: 10.1086/523894.

Knutson, H. A., N. Lewis, J. J. Fortney, A. Burrows, A. P. Showman, N. B. Cowan, E. Agol, S. Aigrain, D. Charbonneau, D. Deming, J.-M. Désert, G. W. Henry, J. Langton, and G. Laughlin (2012). 3.6 and 4.5 μm Phase Curves and Evidence for Non-equilibrium Chemistry in the Atmosphere of Extrasolar Planet HD 189733b. *ApJ*, **754**, 22. doi: 10.1088/0004-637X/754/1/22.

Koen, C. (2005a). I_C and R_C band time-series observations of some bright ultracool dwarfs. *MNRAS*, **360**, pp. 1132–1142. doi: 10.1111/j.1365-2966.2005.09119.x.

Koen, C. (2005b). Time-series observations of the ultracool dwarf SSSPM J0109 - 5101. *MNRAS*, **357**, pp. 1151–1154. doi: 10.1111/j.1365-2966.2005.08654.x.

Kumar, S. S. (1963). The Structure of Stars of Very Low Mass. *ApJ*, **137**, p. 1121. doi: 10.1086/147589.

Kunde, V. G., F. M. Flasar, D. E. Jennings, B. Bézard, D. F. Strobel, B. J. Conrath, C. A. Nixon, G. L. Bjoraker, P. N. Romani, R. K. Achterberg, A. A. Simon-Miller, P. Irwin, J. C. Brasunas, J. C. Pearl, M. D. Smith, G. S. Orton, P. J. Gierasch, L. J. Spilker, R. C. Carlson, A. A. Mamoutkine, S. B. Calcutt, P. L. Read, F. W. Taylor, T. Fouchet, P. Parrish, A. Barucci, R. Courtin, A. Coustenis, D. Gautier, E. Lellouch, A. Marten, R. Prangé, Y. Biraud, C. Ferrari, T. C. Owen, M. M. Abbas, R. E. Samuelson, F. Raulin, P. Ade, C. J. Césarsky, K. U. Grossman, and A. Coradini (2004). Jupiter's Atmospheric Composition from the Cassini Thermal Infrared Spectroscopy Experiment. *Science*, **305**, pp. 1582–1587. doi: 10.1126/science.1100240.

Lane, C., G. Hallinan, R. T. Zavala, R. F. Butler, R. P. Boyle, S. Bourke, A. Antonova, J. G. Doyle, F. J. Vrba, and A. Golden (2007). Rotational Modulation of M/L Dwarfs due to Magnetic Spots. *ApJ*, **668**, pp. L163–L166. doi: 10.1086/523041.

Leahy, D. A., R. F. Elsner, and M. C. Weisskopf (1983). On searches for periodic pulsed emission - The Rayleigh test compared to epoch folding. *ApJ*, **272**, pp. 256–258. doi: 10.1086/161288.

Leggett, S. K., D. Saumon, M. S. Marley, T. R. Geballe, D. A. Golimowski, D. Stephens, and X. Fan (2007). 3.6-7.9 μm Photometry of L and T Dwarfs and the Prevalence of Vertical Mixing in their Atmospheres. *ApJ*, **655**, pp. 1079–1094. doi: 10.1086/510014.

Lewis, J. S. (1969). The clouds of Jupiter and the NH $_3$#58872H $_2$O and NH $_3$#58872H $_2$S systems. *Icarus*, **10**, pp. 365–378. doi: 10.1016/0019-1035(69)90091-8.

Lewis, N. K., H. A. Knutson, A. P. Showman, N. B. Cowan, G. Laughlin, A. Burrows, D. Deming, J. R. Crepp, K. J. Mighell, E. Agol, G. Á. Bakos, D. Charbonneau, J.-M. Désert, D. A. Fischer, J. J. Fortney, J. D. Hartman, S. Hinkley, A. W. Howard, J. A. Johnson, M. Kao, J. Langton, and G. W. Marcy (2013). Orbital Phase Variations of the Eccentric Giant Planet HAT-P-2b. *ApJ*, **766**, 95. doi: 10.1088/0004-637X/766/2/95.

Lodders, K. (2003). Solar System Abundances and Condensation Temperatures of the Elements. *ApJ*, **591**, pp. 1220–1247. doi: 10.1086/375492.

Lodders, K. and B. Fegley, Jr. (2006). *Chemistry of Low Mass Substellar Objects*, p. 1. doi: 10.1007/3-540-30313-8_1.

López Martí, B. and M. R. Zapatero Osorio (2014). Long-term Ks-band photometric monitoring of L dwarfs. *A&A*, **568**, A87. doi: 10.1051/0004-6361/201424141.

Lunine, J. I., W. B. Hubbard, A. Burrows, Y.-P. Wang, and K. Garlow (1989). The effect of gas and grain opacity on the cooling of brown dwarfs. *ApJ*, **338**, pp. 314–337. doi: 10.1086/167201.

Marley, M. S., C. Gelino, D. Stephens, J. I. Lunine, and R. Freedman (1999). Reflected Spectra and Albedos of Extrasolar Giant Planets. I. Clear and Cloudy Atmospheres. *ApJ*, **513**, pp. 879–893. doi: 10.1086/306881.

Marley, M. S. and S. K. Leggett (2009). *The Future of Ultracool Dwarf Science with JWST*, p. 101. doi: 10.1007/978-1-4020-9457-6_4.

Marley, M. S., D. Saumon, and C. Goldblatt (2010). A Patchy Cloud Model for the L to T Dwarf Transition. *ApJ*, **723**, pp. L117–L121. doi: 10.1088/2041-8205/723/1/L117.

McLean, I. S., M. R. McGovern, A. J. Burgasser, J. D. Kirkpatrick, L. Prato, and S. S. Kim (2003). The NIRSPEC Brown Dwarf Spectroscopic Survey. I. Low-Resolution Near-Infrared Spectra. *ApJ*, **596**, pp. 561–586. doi: 10.1086/377636.

Metchev, S., J. Radigan, D. Apai, A. Burgasser, E. Artigau, M. Marley, P. Plavchan, B. Goldman, K. Geissler, and R. Jayawardhana (2011). Weather on Other Worlds: A Survey of Cloud-Induced Variability in Brown Dwarfs. Spitzer Proposal.

Metchev, S. A., A. Heinze, D. Apai, D. Flateau, J. Radigan, A. Burgasser, M. S. Marley, É. Artigau, P. Plavchan, and B. Goldman (2015). Weather on Other Worlds. II. Survey Results: Spots are Ubiquitous on L and T Dwarfs. *ApJ*, **799**, 154. doi: 10.1088/0004-637X/799/2/154.

Mighell, K. J. (2005). Stellar photometry and astrometry with discrete point spread functions. *MNRAS*, **361**, pp. 861–878. doi: 10.1111/j.1365-2966.2005.09208.x.

Mohanty, S., G. Basri, F. Shu, F. Allard, and G. Chabrier (2002). Activity in Very Cool Stars: Magnetic Dissipation in Late M and L Dwarf Atmospheres. *ApJ*, **571**, pp. 469–486. doi: 10.1086/339911.

Nakajima, T., B. R. Oppenheimer, S. R. Kulkarni, D. A. Golimowski, K. Matthews, and S. T. Durrance (1995). Discovery of a cool brown dwarf. *Nature*, **378**, pp. 463–465. doi: 10.1038/378463a0.

Noll, K. S., T. R. Geballe, S. K. Leggett, and M. S. Marley (2000). The Onset of Methane in L Dwarfs. *ApJ*, **541**, pp. L75–L78. doi: 10.1086/312906.

Perryman, M. A. C., A. G. A. Brown, Y. Lebreton, A. Gomez, C. Turon, G. Cayrel de Strobel, J. C. Mermilliod, N. Robichon, J. Kovalevsky, and F. Crifo (1998). The Hyades: distance, structure, dynamics, and age. *A&A*, **331**, pp. 81–120.

Radigan, J. (2014). An Independent Analysis of the Brown Dwarf Atmosphere Monitoring (BAM) Data: Large-amplitude Variability is Rare Outside the L/T Transition. *ApJ*, **797**, 120. doi: 10.1088/0004-637X/797/2/120.

Radigan, J., R. Jayawardhana, D. Lafrenière, É. Artigau, M. Marley, and D. Saumon (2012). Large-amplitude Variations of an L/T Transition Brown Dwarf: Multi-wavelength Observations of Patchy, High-contrast Cloud Features. *ApJ*, **750**, 105. doi: 10.1088/0004-637X/750/2/105.

Rayner, J. T., M. C. Cushing, and W. D. Vacca (2009). The Infrared Telescope Facility (IRTF) Spectral Library: Cool Stars. *ApJS*, **185**, pp. 289–432. doi: 10.1088/0067-0049/185/2/289.

Rayner, J. T., D. W. Toomey, P. M. Onaka, A. J. Denault, W. E. Stahlberger, W. D. Vacca, M. C. Cushing, and S. Wang (2003). SpeX: A Medium-Resolution 0.8-5.5 Micron Spectrograph and Imager for the NASA Infrared Telescope Facility. *PASP*, **115**, pp. 362–382. doi: 10.1086/367745.

Reach, W. T., S. T. Megeath, M. Cohen, J. Hora, S. Carey, J. Surace, S. P. Willner, P. Barmby, G. Wilson, W. Glaccum, P. Lowrance, M. Marengo, and G. G. Fazio (2005). Absolute Calibration of the Infrared Array Camera on the Spitzer Space Telescope. *PASP*, **117**, pp. 978–990. doi: 10.1086/432670.

Reid, I. N., K. L. Cruz, J. D. Kirkpatrick, P. R. Allen, F. Mungall, J. Liebert, P. Lowrance, and A. Sweet (2008). Meeting the Cool Neighbors. X. Ultracool Dwarfs from the 2MASS All-Sky Data Release. *AJ*, **136**, pp. 1290–1311. doi: 10.1088/0004-6256/136/3/1290.

Reid, I. N., J. D. Kirkpatrick, J. E. Gizis, C. C. Dahn, D. G. Monet, R. J. Williams, J. Liebert, and A. J. Burgasser (2000). Four Nearby L Dwarfs. *AJ*, **119**, pp. 369–377. doi: 10.1086/301177.

Reid, I. N., E. Lewitus, P. R. Allen, K. L. Cruz, and A. J. Burgasser (2006). A Search for Binary Systems among the Nearest L Dwarfs. *AJ*, **132**, pp. 891–901. doi: 10.1086/505626.

Robinson, T. D. and M. S. Marley (2014). Temperature Fluctuations as a Source of Brown Dwarf Variability. *ApJ*, **785**, 158. doi: 10.1088/0004-637X/785/2/158.

Route, M. and A. Wolszczan (2012). The Arecibo Detection of the Coolest Radio-flaring Brown Dwarf. *ApJ*, **747**, L22. doi: 10.1088/2041-8205/747/2/L22.

Saumon, D. and M. S. Marley (2008). The Evolution of L and T Dwarfs in Color-Magnitude Diagrams. *ApJ*, **689**, pp. 1327–1344. doi: 10.1086/592734.

Saumon, D., M. S. Marley, M. C. Cushing, S. K. Leggett, T. L. Roellig, K. Lodders, and R. S. Freedman (2006). Ammonia as a Tracer of Chemical Equilibrium in the T7.5 Dwarf Gliese 570D. *ApJ*, **647**, pp. 552–557. doi: 10.1086/505419.

Scargle, J. D. (1982). Studies in astronomical time series analysis. II - Statistical aspects of spectral analysis of unevenly spaced data. *ApJ*, **263**, pp. 835–853. doi: 10.1086/160554.

Schwarzenberg-Czerny, A. (1989). On the advantage of using analysis of variance for period search. *MNRAS*, **241**, pp. 153–165.

Showman, A. P., J. Y.-K. Cho, and K. Menou (2010). *Atmospheric Circulation of Exoplanets*, pp. 471–516. University of Arizona Press.

Showman, A. P. and T. E. Dowling (2000). Nonlinear Simulations of Jupiter's 5-Micron Hot Spots. *Science*, **289**, pp. 1737–1740. doi: 10.1126/science.289.5485.1737.

Showman, A. P. and Y. Kaspi (2013). Atmospheric Dynamics of Brown Dwarfs and Directly Imaged Giant Planets. *ApJ*, **776**, 85. doi: 10.1088/0004-637X/776/2/85.

Skrutskie, M. F., R. M. Cutri, R. Stiening, M. D. Weinberg, S. Schneider, J. M. Carpenter, C. Beichman, R. Capps, T. Chester, J. Elias, J. Huchra, J. Liebert, C. Lonsdale, D. G. Monet, S. Price, P. Seitzer, T. Jarrett, J. D. Kirkpatrick, J. E. Gizis, E. Howard, T. Evans, J. Fowler, L. Fullmer, R. Hurt, R. Light, E. L. Kopan, K. A. Marsh, H. L. McCallon, R. Tam, S. Van Dyk, and S. Wheelock (2006). The Two Micron All Sky Survey (2MASS). *AJ*, **131**, pp. 1163–1183. doi: 10.1086/498708.

Stephens, D. C., S. K. Leggett, M. C. Cushing, M. S. Marley, D. Saumon, T. R. Geballe, D. A. Golimowski, X. Fan, and K. S. Noll (2009). The 0.8-14.5 μm Spectra of Mid-L to Mid-T Dwarfs: Diagnostics of Effective Temperature, Grain Sedimentation, Gas Transport, and Surface Gravity. *ApJ*, **702**, pp. 154–170. doi: 10.1088/0004-637X/702/1/154.

Stringfellow, G. S. (1989). *Evolutionary scenarios for low-mass stars and substellar brown dwarfs*. Ph.D. thesis, California Univ., Santa Cruz.

Stumpf, M. B., W. Brandner, V. Joergens, T. Henning, H. Bouy, R. Köhler, and M. Kasper (2010). The Search for Planetary Mass Companions to Field Brown Dwarfs with HST/NICMOS. *ApJ*, **724**, pp. 1–11. doi: 10.1088/0004-637X/724/1/1.

Tinney, C. G., A. J. Burgasser, and J. D. Kirkpatrick (2003). Infrared Parallaxes for Methane T Dwarfs. *AJ*, **126**, pp. 975–992. doi: 10.1086/376481.

Toon, O. B., C. P. McKay, T. P. Ackerman, and K. Santhanam (1989). Rapid calculation of radiative heating rates and photodissociation rates in inhomogeneous multiple scattering atmospheres. *J. Geophys. Res.*, **94**, pp. 16287–16301. doi: 10.1029/JD094iD13p16287.

Vasavada, A. R. and A. P. Showman (2005). Jovian atmospheric dynamics: an update after Galileo and Cassini. *Reports on Progress in Physics*, **68**, pp. 1935–1996. doi: 10.1088/0034-4885/68/8/R06.

Vrba, F. J., A. A. Henden, C. B. Luginbuhl, H. H. Guetter, J. A. Munn, B. Canzian, A. J. Burgasser, J. D. Kirkpatrick, X. Fan, T. R. Geballe, D. A. Golimowski, G. R. Knapp, S. K. Leggett, D. P. Schneider, and J. Brinkmann (2004). Preliminary Parallaxes of 40 L and T Dwarfs from the US Naval Observatory Infrared Astrometry Program. *AJ*, **127**, pp. 2948–2968. doi: 10.1086/383554.

Westphal, J. A. (1969). Observations of localised 5-micron radiation from Jupiter. *ApJ*, **157**, pp. L63–L64. doi: 10.1086/180386.

Wilson, P. A., A. Rajan, and J. Patience (2014). The brown dwarf atmosphere monitoring (BAM) project. I. The largest near-IR monitoring survey of L and T dwarfs. *A&A*, **566**, A111. doi: 10.1051/0004-6361/201322995.

Yang, H., D. Apai, M. S. Marley, D. Saumon, C. V. Morley, E. Buenzli, É. Artigau, J. Radigan, S. Metchev, A. J. Burgasser, S. Mohanty, P. J. Lowrance, A. P. Showman, T. Karalidi, D. Flateau, and A. N. Heinze (2015). HST Rotational Spectral Mapping of Two L-type Brown Dwarfs: Variability in and out of Water Bands indicates High-altitude Haze Layers. *ApJ*, **798**, L13. doi: 10.1088/2041-8205/798/1/L13.

York, D. G., J. Adelman, J. E. Anderson, Jr., S. F. Anderson, J. Annis, N. A. Bahcall, J. A. Bakken, R. Barkhouser, S. Bastian, E. Berman, W. N. Boroski, S. Bracker, C. Briegel, J. W. Briggs, J. Brinkmann, R. Brunner, S. Burles, L. Carey, M. A. Carr, F. J. Castander, B. Chen, P. L. Colestock, A. J. Connolly, J. H. Crocker, I. Csabai, P. C. Czarapata, J. E. Davis, M. Doi, T. Dombeck, D. Eisenstein, N. Ellman, B. R. Elms, M. L. Evans, X. Fan, G. R. Federwitz, L. Fiscelli, S. Friedman, J. A. Frieman, M. Fukugita, B. Gillespie, J. E. Gunn, V. K. Gurbani, E. de Haas, M. Haldeman, F. H. Harris, J. Hayes, T. M. Heckman, G. S. Hennessy, R. B. Hindsley, S. Holm, D. J. Holmgren, C.-h. Huang, C. Hull, D. Husby, S.-I. Ichikawa, T. Ichikawa, Ž. Ivezić, S. Kent, R. S. J. Kim, E. Kinney, M. Klaene, A. N. Kleinman, S. Kleinman, G. R. Knapp, J. Korienek, R. G. Kron, P. Z. Kunszt, D. Q. Lamb, B. Lee, R. F. Leger, S. Limmongkol, C. Lindenmeyer, D. C. Long, C. Loomis, J. Loveday, R. Lucinio, R. H. Lupton, B. MacKinnon, E. J. Mannery, P. M. Mantsch, B. Margon, P. McGehee, T. A. McKay, A. Meiksin, A. Merelli, D. G. Monet, J. A. Munn, V. K. Narayanan, T. Nash, E. Neilsen, R. Neswold, H. J. Newberg, R. C. Nichol, T. Nicinski, M. Nonino, N. Okada, S. Okamura, J. P. Ostriker, R. Owen, A. G. Pauls, J. Peoples, R. L. Peterson, D. Petravick, J. R. Pier, A. Pope, R. Pordes, A. Prosapio, R. Rechenmacher, T. R. Quinn, G. T. Richards, M. W. Richmond, C. H. Rivetta, C. M. Rockosi, K. Ruthmansdorfer, D. Sandford, D. J. Schlegel, D. P. Schneider, M. Sekiguchi, G. Sergey, K. Shimasaku, W. A. Siegmund, S. Smee, J. A. Smith, S. Snedden, R. Stone, C. Stoughton, M. A. Strauss, C. Stubbs, M. SubbaRao, A. S. Szalay, I. Szapudi, G. P. Szokoly, A. R. Thakar, C. Tremonti, D. L. Tucker, A. Uomoto, D. Vanden Berk, M. S. Vogeley, P. Waddell, S.-i. Wang, M. Watanabe, D. H. Weinberg, B. Yanny, N. Yasuda, and SDSS Collaboration (2000). The Sloan Digital Sky Survey: Technical Summary. *AJ*, **120**, pp. 1579–1587. doi: 10.1086/301513.

Zapatero Osorio, M. R., V. J. S. Béjar, P. A. Miles-Páez, K. Peña Ramírez, R. Rebolo, and E. Pallé (2014). Trigonometric parallaxes of young field L dwarfs. *A&A*, **568**, A6. doi: 10.1051/0004-6361/201321340.

Zapatero Osorio, M. R., E. L. Martín, H. Bouy, R. Tata, R. Deshpande, and R. J. Wainscoat (2006). Spectroscopic Rotational Velocities of Brown Dwarfs. *ApJ*, **647**, pp. 1405–1412. doi: 10.1086/505484.

Zhang, X. and A. P. Showman (2014). Atmospheric Circulation of Brown Dwarfs: Jets, Vortices, and Time Variability. *ApJ*, **788**, L6. doi: 10.1088/2041-8205/788/1/L6.